

2014

## Superconducting Thin Films for SRF Cavity Applications: A Route to Higher Field Gradient Linacs

William Michael Roach  
*College of William & Mary - Arts & Sciences*

Follow this and additional works at: <https://scholarworks.wm.edu/etd>



Part of the [Condensed Matter Physics Commons](#), and the [Materials Science and Engineering Commons](#)

---

### Recommended Citation

Roach, William Michael, "Superconducting Thin Films for SRF Cavity Applications: A Route to Higher Field Gradient Linacs" (2014). *Dissertations, Theses, and Masters Projects*. Paper 1539623638.  
<https://dx.doi.org/doi:10.21220/s2-sehr-gm86>

This Dissertation is brought to you for free and open access by the Theses, Dissertations, & Master Projects at W&M ScholarWorks. It has been accepted for inclusion in Dissertations, Theses, and Masters Projects by an authorized administrator of W&M ScholarWorks. For more information, please contact [scholarworks@wm.edu](mailto:scholarworks@wm.edu).

**Superconducting Thin Films for SRF Cavity Applications:  
a Route to Higher Field Gradient Linacs**

**William Michael Roach**

**Chesterfield, VA**

**Master of Science, The College of William and Mary, 2011  
Bachelor of Science, Virginia Commonwealth University, 2009**

**A Dissertation presented to the Graduate Faculty  
of the College of William and Mary in Candidacy for the Degree of  
Doctor of Philosophy**

**Applied Science**

**The College of William and Mary  
January 2014**

# APPROVAL PAGE

This Dissertation is submitted in partial fulfillment of  
the requirements for the degree of

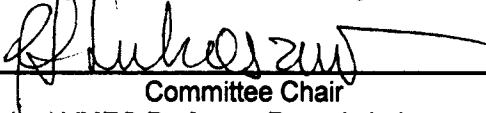
Doctor of Philosophy



---

William Michael Roach

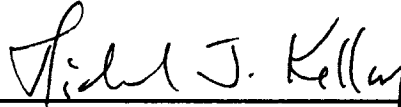
Approved by the Committee, August 2013



---

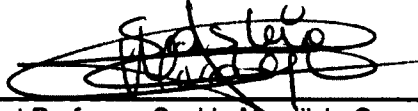
Committee Chair

Distinguished VMEC Professor Rosa A. Lukaszew, Physics  
The College of William and Mary



---

Professor Michael J. Kelley, Applied Science  
The College of William and Mary



---

Research Assistant Professor Saskia Mordijck, Computer Science  
The College of William and Mary



---

Dr. Charles E. Reece  
Thomas Jefferson National Accelerator Facility

## ABSTRACT

Many linear accelerator (linac) applications rely on the use of superconducting radio frequency (SRF) cavities. In order to overcome the current field gradient limits imposed by the use of bulk niobium, a model involving the deposition of alternating superconducting-insulating-superconducting (SIS) thin films onto the interior surface of SRF cavities has been proposed. Since SRF performance is a surface phenomenon, the critical surface of these cavities is less than 1 micron thick, thus enabling the use of thin films. Before such approach can successfully be implemented fundamental studies correlating the microstructure and superconducting properties of thin films are needed. To this end the effect of grain boundary density and interfacial strain in thin films has been explored. Thin films with a smaller grain boundary density were found to have better superconducting properties than films with a larger grain boundary density. Interfacial strain due to a lattice mismatch between the film and substrate lead to two regions in films, one strained region near the interface and one relaxed region away from the interface. The presence of two regions in the film resulted in two types of superconducting behavior. Niobium films were deposited onto copper surfaces to help understand why previous attempts of implementing niobium coated copper cavities in order to exploit the better thermal properties of copper had varying degrees of success. It was found that an increased growth temperature produced niobium films with larger grains and correspondingly better superconducting properties. Proof of principle multilayer samples were prepared to test the SIS model. For the first time, multilayers were produced that were capable of shielding an underlying niobium film from vortex penetration beyond the lower critical field of bulk niobium. This result provides evidence supporting the feasibility of the SIS model.

## TABLE OF CONTENTS

Acknowledgements.....	ii
Dedication.....	iii
1 Introduction.....	1
2 Superconductivity and SRF Cavities.....	8
3 Fabrication and Characterization.....	27
4 Superconducting Thin Films and Multilayers.....	56
5 Summary and Outlook.....	96
Bibliography.....	103

## ACKNOWLEDGEMENTS

I am extremely grateful to all the people who have helped or supported me during the completion of this dissertation. First and foremost, I want to express my appreciation for my advisor, Ale Lukaszew. Her constant encouragement and guidance helped me become the scholar that I am today. I am also thankful for the help received from both current and former members of the Lukaszew research group who assisted with various experiments and lab activities. These include Dr. César Clavero, Dr. Jonathan Skuza, Kaida Yang, Douglas Beringer, Lei Wang, Zhaozhu Li, and Jose Riso.

The research presented in the dissertation would not have been possible without the ongoing collaboration with Larry Phillips, Anne-Marie Valente-Feliciano, Josh Spradlin, Xin Zhao, Grigory Eremeev, Stuart Wolf, Jiwei Lu, Dale Batchelor, and Ka Wong. Additionally, funding for this work was provided by the Defense Threat Reduction Agency, the Department of Energy, the Virginia Space Grant Consortium, and William and Mary Arts and Sciences.

The Applied Science staff, Lydia Whitaker, Rosi Fox, and Destiny Elliot, have provided never ending support as well as friendly conversations throughout my entire time as William and Mary.

I am especially thankful for the members of my dissertation committee, Michael Kelley, Charlie Reece, and Saskia Mordijck for the useful feedback provided.

I would not be where I am today if I did not have constant love and support from my family throughout the many years that it took me to reach this point.

Last and certainly not least, I am forever indebted to my wonderful wife, Vanessa. You have always stood by me and believed in me, even in times when I did not believe in myself.

This dissertation is dedicated to my wife, Vanessa.

# Chapter 1

## Introduction

Particle accelerators are essential tools in the investigation of subatomic particles and are also of interest in defense applications. A key component of high energy linear accelerator technology is the electromagnetic cavity resonating at a microwave frequency leading to energy gained by charged particles. In terms of material choice, superconducting materials offer the advantage of reduced losses under radio frequency (RF) fields. Niobium is the material most often utilized in superconducting radio frequency (SRF) accelerator applications. Recent advances in niobium cavity technology have significantly increased the maximum breakdown electric field to 35-50 MV/m which is approaching the theoretical limit for bulk niobium. The RF fields has a magnetic component that is parallel to the cavity's surface. Superconductors like niobium can only withstand a certain maximum applied magnetic field before magnetic vortices enter the material, causing a significant decrease in cavity performance. Therefore, the maximum electric field that can be sustained is limited by how much



magnetic field the cavity material can withstand. Further breakthroughs in SRF cavity technology can only be achieved by using new materials, new surface treatments, or coating techniques to overcome the intrinsic limits of bulk niobium technology. With new materials incorporated into SRF cavities, it may be possible to achieve accelerating gradients as high as 100 MV/m or increase the operating temperatures from 2K to 4.2K with a significant reduction of the refrigeration cost. Therefore, further optimization of the material cost and energy consumption of future particle accelerators depends on the development of new materials and the engineering of the active surfaces in accelerator cavities.

Because the penetration of RF fields into superconducting materials is very shallow ( $<1\mu\text{m}$ ), SRF properties are inherently a surface phenomenon which enables the use of thin films to alter the active surface in SRF cavities. Due to their inherent geometry, thin films would constitute the active surface. Since there is strong correlation between a material's microstructure, surface morphology, and superconducting properties, systematic work must be carried out for superconducting thin films to be able to perform as close as possible to bulk materials. It may also be possible to combine thin films and materials other than niobium in structures that can outperform bulk materials.

While there are still systematic studies that need to be completed, there are several material factors that contribute to degraded SRF performance with respect to ideal surfaces. For example,

- The presence of intragranular impurities contributes to a reduction of the elec-

tron mean free path, which reduces the local lower critical field,  $H_{C1}$ , the magnetic field at which magnetic flux first penetrates a Type-II superconductor in the form of vortices [1],

- Lattice defects between crystallographic grains also contribute to electron scattering sites [2],
- Lattice mismatch occurring at grain boundaries may also be a contributing factor to localization of impurities and lossy oxidation states [2],
- The presence and diffusion of impurities at grain boundaries and intergranular oxidation states contribute weak links to the flow of surface currents in superconductors, creating a non-linear loss mechanism [3],
- A rough surface topography contributes to local field enhancements, which effectively allows early vortex entry and thus increased dissipation [4],
- Chemical processing aimed at improving the surface quality may leave localized lossy oxides that increase the local temperature leading to non-linear dissipation [5].

Thus, fundamental work is needed to understand the actual correlation between detailed material characteristics and the subsequent SRF performance. For this approach, other superconducting materials with a superconducting transition temperature,  $T_C$ , higher than  $T_C^{Nb} = 9.2$  K offer several advantages as described below. We note that for a superconducting material to be a good candidate for SRF cavities, it

also needs to have low resistivity in the normal state in order to minimize RF losses. Furthermore, to maximize accelerating gradients, a high thermodynamic critical field,  $H_C$ , and a high lower critical field,  $H_{C1}$ , are necessary.

Materials with  $T_C > T_C^{Nb}$  are desirable due to their theoretically lower surface resistance and higher operating temperature. In the framework of the BCS theory of superconductivity (see Chapter 2 for an expanded discussion), the surface resistance,  $R_{surf}$ , can be described as

$$R_{surf} = A\omega^2 \exp\left(-\frac{\Delta(0)}{k_B T}\right) + R_{res} \quad (1.1)$$

where  $A$  is a material related constant,  $\omega$  is operating frequency,  $\Delta$  is the superconducting energy gap,  $k_B$  is the Boltzmann constant, and  $T$  is temperature. One important relationship to take note of in Equation (1.1) is that

$$R_{surf} \propto \exp\left(-\frac{\Delta(0)}{k_B T}\right). \quad (1.2)$$

BCS theory also gives us a relationship between  $\Delta$  and  $T_C$  that follows

$$\Delta(0) = 1.76k_B T_C \quad (1.3)$$

which combined with Equation (1.2) gives

$$R_{surf} \propto \exp\left(-\frac{1.76T_C}{T}\right). \quad (1.4)$$

The consequence of this is that  $R_{surf}$  decreases strongly for higher  $T_C$  materials. In fact, Equation (1.4) implies that a superconductor with  $T_C > 20$  at 4.2 K should have a similar  $R_{surf}$  to bulk niobium at 2 K since

$$\frac{20}{4.2} \approx \frac{9.2}{2}. \quad (1.5)$$

Niobium's dominance in SRF applications is due to its highest  $T_C$  and  $H_{C1}$  of all pure metals. Many compounds, including the high  $T_C$  class of superconductors containing cuprates such as yttrium barium copper oxide (YBCO) and bismuth strontium calcium copper oxide (BSCCO), have  $T_C$  and  $H_C$  values larger than niobium, although their  $H_{C1}$  values are lower than niobium. The high  $T_C$  cuprates are not considered viable candidates for SRF applications for a number of reasons. First, the coherence lengths in these cuprates are very short, leading to a high sensitivity to defects. Second, these materials have a large anisotropy of magnetic and electrical properties depending on which direction the properties are being measured along. Due to this anisotropy, it would be ideal to have the same crystallographic plane normal to the surface of the cavity which is difficult considering the cavity geometries. Finally, the d-wave nature of the electron pairing in the cuprates will lead to a larger  $R_S$  than s-wave superconductors.

In order to overcome the limits of bulk niobium and taking advantage of the ability to use thin films, a model has been proposed that involves coating the interior surface of SRF cavities with a multilayered film structure involving suitable

superconducting layers with adequate thickness that would shield the cavity from higher magnetic fields, allowing for larger accelerating gradients to be achieved [6]. The challenge of implementing this model has been to understand the dependence of SRF performance on the material properties in thin film coatings. As stated above, in addition to increasing the accelerating gradient of cavities, it is also desirable to improve their thermal efficiency while also lowering fabrication costs by for example applying superconductor coatings to good thermal conductor materials such as copper or aluminum. Therefore, fundamental studies that correlate the microstructure of thin films and their resulting superconducting properties are necessary for successful implementation of thin film coatings in the next generation of SRF cavities. With this understanding, appropriate techniques can be employed to tailor the surface for greatest benefit.

This dissertation presents a comprehensive collection of systematic studies on thin film niobium on both insulating and metal surfaces that examine the relationship between the microstructure of niobium films and their superconducting properties throughout the initial stages of growth, which in turn depend on the epitaxy of the film onto the underlying surface. Additional work showing the growth and characterization of niobium nitride thin films and multilayers and their potential use in SRF cavities is also described.

The contents of this dissertation are organized as follows. Chapter 2 introduces the basic physics of superconductivity as well as the operation and current state of superconducting accelerator technology. A theoretical proposal to overcome the limits

of current technology is also discussed. Chapter 3 describes the material fabrication and characterization methods that were utilized for these studies. Chapter 4 presents the results of structure-property correlated studies carried out on superconducting thin film samples. Specifically the effects of grain boundary density in niobium films on both insulating and metallic surfaces are explored. The effects of the film-substrate interface on the resulting superconducting properties are analyzed. The fabrication and characterization of niobium nitride thin films and multilayered structures are presented providing results that support the validity of the model described in Chapter 2. It is important to point out that this work led to the demonstration of magnetic field shielding above that of bulk Nb, reported for the first time in 2012. Finally, Chapter 5 summarizes the important results of this dissertation and provides a road map for continued work on this topic.

# Chapter 2

## Superconductivity and SRF

### Cavities

#### 2.1 Superconductivity

Superconductivity is a phenomenon that manifests as a decrease of the DC electrical resistance to zero below a critical temperature,  $T_C$ , for some specific materials called superconductors. The resistance of a normal conductor will decrease as temperature decreases, but to a finite value. A comparison of the resistive behavior at low temperatures is shown in Figure 2.1. Superconductivity was discovered in 1911 by Kamerlingh Onnes shortly after he developed the technology necessary to liquefy helium [7]. File and Mills later determined experimentally that it would take at least 100,000 years for a current in a superconducting solenoid to decay [8]. In 1933, Meissner and Ochsenfeld made an important discovery regarding the magnetic behavior of

a superconductor compared to a perfect conductor (i.e. a conductor whose electron mean free path is infinite) [9]. When a perfect conductor is placed in a small magnetic field, the field can penetrate completely into the material. Cooling the perfect conductor down to low temperatures has no effect on the penetration of the magnetic field. On the other hand, a superconductor placed in a small magnetic field would experience field penetration above its  $T_C$ , while below  $T_C$  the superconductor exhibits perfect diamagnetism and expels all magnetic field as shown in Figure 2.2. This behavior is called the Meissner effect.

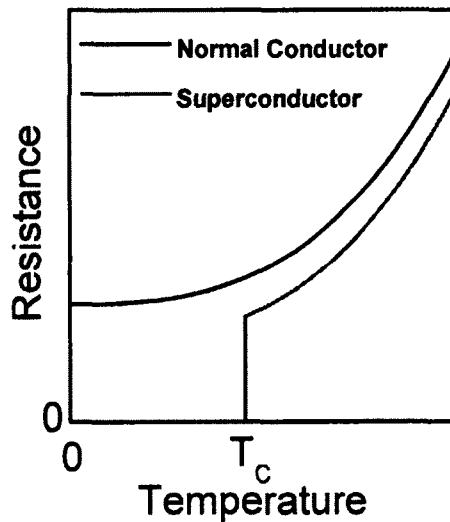


Figure 2.1: Comparison of low temperature resistance for a normal conductor and a superconductor.

In 1935, Fritz and Heinz London developed their namesake equations that further described the magnetic behavior of superconducting materials [10]. The first London equation (2.1) is derived from the Drude-Lorentz equation for the motion of electrons in a metal, with modifications to include the perfect conducting behavior of a su-



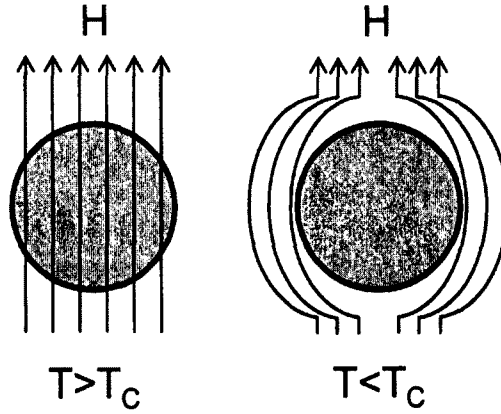


Figure 2.2: Diagram of the Meissner effect.

perconductor affecting the viscous drag term. In (2.1),  $\mathbf{j}$  is the current density,  $n$  is the conduction electron density,  $e$  is the charge of an electron,  $m$  is the mass of an electron, and  $\mathbf{E}$  is an electric field. Taking the curl of the time derivative of Maxwell's fourth equation and using (2.1) to model a perfect conductor, and excluding the time independent field solutions in order to agree with the experimental observations of the Meissner effect, the second London equation is found to be (2.2).

$$\frac{d\mathbf{j}}{dt} = \frac{ne^2}{m}\mathbf{E} \quad (2.1)$$

$$\nabla \times (\nabla \times \mathbf{H}) + \left( \frac{1}{\lambda_L^2} + \frac{\varepsilon}{c^2} \frac{\partial^2}{\partial t^2} \right) \mathbf{H} = 0 \quad (2.2)$$

The term  $\lambda_L$  is known as the London penetration depth and is defined as

$$\lambda_L = \sqrt{\frac{mc^2}{4\pi ne^2}}. \quad (2.3)$$

This characteristic depth determines the decay of the magnetic field magnitude inside a superconducting material and follows (2.4). Figure 2.3 provides a visual representation of the attenuation of a magnetic field as it enters a superconductor.

$$H(x) = H_0 e^{-\frac{x}{\lambda_L}} \quad (2.4)$$

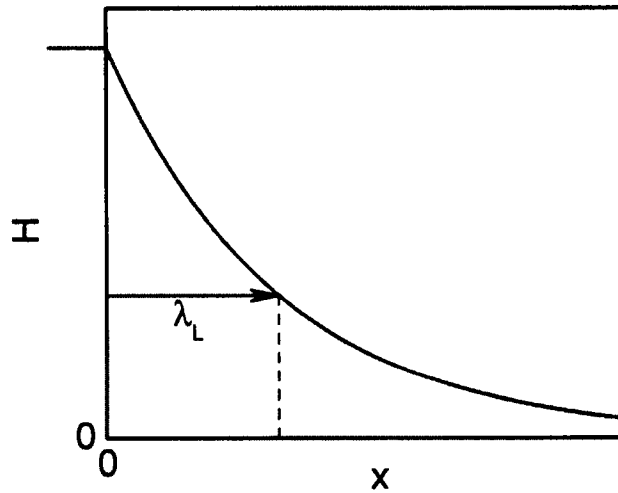


Figure 2.3: Magnetic field magnitude as a function of distance from the surface.

The London penetration depth is temperature dependent and approaches  $\infty$ , corresponding to full penetration into the material, as the temperature approaches  $T_C$  in agreement with (2.5). Figure 2.4 provides a visual representation of the temperature dependent behavior of the London penetration depth. Unlike the penetration depth of electromagnetic waves due to the skin effect, the London penetration depth is not frequency dependent.

$$\lambda_L(T) = \frac{\lambda_L(0)}{\sqrt{1 - \left(\frac{T}{T_c}\right)^4}} \quad (2.5)$$

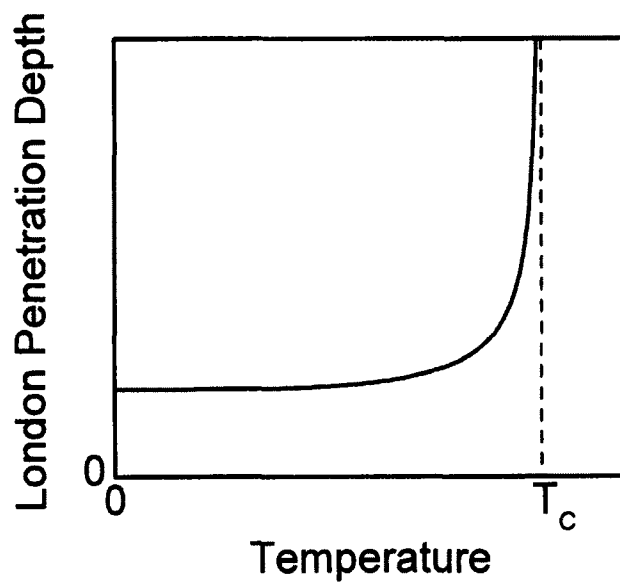


Figure 2.4: London penetration depth as a function of temperature.

As experimental work on superconducting materials continued, two categories of superconductors (Type I and Type II) emerged depending on their response to an externally applied magnetic field. When an increasing magnetic field is applied, Type I superconductors remain in the Meissner state until a critical field,  $H_C$ , is reached which forces the material back into the normal state. In 1937, Shubnikov *et al.* discovered that some superconductors experience a mixed phase between the superconducting and normal state [11]. Superconducting materials where a mixed phase is allowed are called Type II superconductors. Because Type II superconductors have three phases (Meissner, mixed, and normal), they are characterized by two critical fields. The lower critical field,  $H_{C1}$ , is the field at which the material switches from the Meissner phase to the mixed phase and the upper critical field,  $H_{C2}$ , corresponds to the material leaving the mixed phase and behaving as the normal phase. In the mixed phase, magnetic flux is allowed to penetrate into the material in tightly confined regions called vortices. The theory of these quantized flux lines was later developed by Abrikosov [12] (the vortices are sometimes referred to as “Abrikosov vortices”) and experimental images of the vortices were first obtained by Essmann and Träuble [13][14]. The generalized magnetic response of Type I and Type II superconductors is shown in Figure 2.5.

In order to better understand the difference between Type I and Type II, a second characteristic length called the coherence length,  $\xi$ , was proposed by Ginzburg and Landau [15] as well as Pippard [16]. The coherence length was described as the spatial response of a superconductor to a perturbation, such as the interface between a nor-

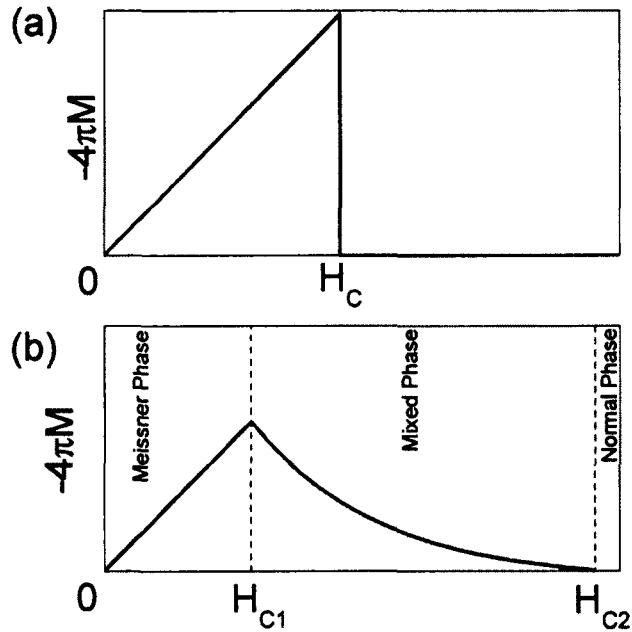


Figure 2.5: Magnetization as a function of applied field for (a) Type I and (b) Type II superconductors.

mal conductor and a superconductor. Despite similar length scales, the Pippard and Ginzburg-Landau coherence lengths are not identical. In general, when the coherence length of a superconductor is larger than its London penetration depth, it will behave like a Type I superconductor. Type II superconductors generally have a larger London penetration depth than coherence length. Figure 2.6 provides a graphical representation of the relationship between superconductor type, London penetration depth, and coherence length.

A more precise method for determining a superconductor type uses the Ginzburg-Landau parameter

$$\kappa = \frac{\lambda_L}{\xi} \quad (2.6)$$

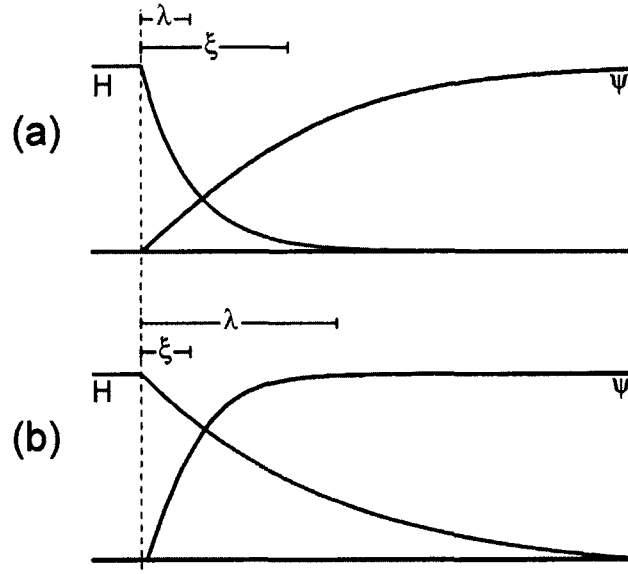


Figure 2.6: Relationship between the London penetration depth and the coherence length for (a) Type I and (b) Type II superconductors. The dashed line represents the surface of a superconductor.

where the exact regimes for a Type I and Type II superconductors are defined by

$$\text{Type I: } \kappa < \frac{1}{\sqrt{2}} \quad (2.7)$$

$$\text{Type II: } \kappa > \frac{1}{\sqrt{2}}.$$

Additionally, the London penetration depth and coherence lengths can be used to calculate a superconductor's theoretical critical fields:  $H_C$  (critical field for Type I or thermodynamic critical field),  $H_{C1}$  (lower critical field for Type II), and  $H_{C2}$  (upper critical field for Type II) as

$$H_C = \frac{\phi_0}{2\sqrt{2}\pi\lambda_L\xi}, \quad (2.8)$$

$$H_{C1} = \frac{\phi_0}{4\pi\lambda_L^2} \ln\left(\frac{\lambda_L}{\xi}\right), \quad (2.9)$$

$$H_{C2} = \frac{\phi_0}{2\pi\xi^2} \quad (2.10)$$

[17]. The  $\phi_0$  term in these equations represents the flux quantum, or the amount of magnetic flux passing through each individual vortex in the mixed phase.

The first microscopic theory of superconductivity was presented by Bardeen, Cooper, and Schrieffer [18] [19] and is commonly referred as the BCS theory. The foundation of the BCS theory of superconductivity is the idea that two electrons can form what is known as a Cooper pair. At the low temperature required for superconductivity, lattice vibrations (phonons) are minimal. As such, an electron traveling through a metal can cause a lattice distortion due to Coulombic attraction with the positively charged ion cores. This lattice distortion creates a small area with a net positive charge that attracts another electron in the material. This electron-lattice-electron interaction creates two electrons that are paired in a boson-like state, called a Cooper pair, which can occupy the same electronic quantum state. In BCS theory, the coherence length,  $\xi$ , is interpreted as the average size of the Cooper pair. For a pure superconductor,  $\xi$  typically has a value of 100-1000 nm. For impure superconductors,  $\xi$  will decrease as the mean free path,  $l$ , decreases.

Unlike the DC case, superconductors in AC applications suffer from power dissipation due to surface resistance described by

$$R_{surf} = R_{BCS} + R_{res} \quad (2.11)$$

where  $R_{BCS}$  is the BCS resistance term and  $R_{res}$  is the residual resistance due to defects and impurities.  $R_{res}$  is commonly observed to be temperature independent and is typically only a few  $n\Omega$  for clean niobium. In AC applications, electromagnetic waves penetrate a thin layer at the surface and interact with electrons that are not bound or in Cooper pairs. The motion and scattering of these unbound electrons is the source of  $R_{surf}$ . Using the two fluid model (a supercurrent due to the Cooper pairs and a normal current due to the unbound electrons), the  $R_{BCS}$  term may be described as

$$R_{BCS} \propto \left( \lambda_L \sqrt{1 + \frac{\xi}{l}} \right)^3 \omega^2 l \exp\left(\frac{-1.76T_C}{T}\right). \quad (2.12)$$

A complete derivation of this term can be found in reference [20]. There is a great deal to learn about the resistance found in AC superconducting applications using (2.12). The resistance is exponentially dependent on temperature and proportional to the square of the operating frequency. The dependence of the resistance on the mean free path,  $l$ , and the coherence length,  $\xi$ , reveals an interesting point about the conditions necessary to achieve the minimal resistance. The minimum resistance does not occur for very pure superconductors, where  $l \gg \xi$ , but instead occurs when the mean free path and coherence length approach the same value,  $l \approx \xi$ . Both theoretical models and experimental observations have supported this point [21] [22].



There is also an additional critical field to be considered in the AC case that was not present in the DC case. This field is called the superheating field,  $H_{sh}$ . A superheated Type II superconductor may remain in a metastable Meissner state above  $H_{C1}$  up to  $H_{sh}$ . The exact value of  $H_{sh}$  depends on  $\kappa$  following

$$\begin{aligned}
H_{sh} &\approx \frac{0.89}{\sqrt{\kappa}} H_C & \text{for } \kappa \ll 1, \\
H_{sh} &\approx 1.2 H_C & \text{for } \kappa \approx 1, \\
H_{sh} &\approx 0.75 H_C & \text{for } \kappa \gg 1,
\end{aligned}
\tag{2.13}$$

as calculated in reference [23].  $H_{sh}$  arises from an entropy discontinuity and nucleation centers for a superconductor in the presence of an external magnetic field. Because it is theoretically possible to maintain a metastable Meissner state up to  $H_{sh}$ , it is expected that the critical RF field is equal to  $H_{sh}$  [5] and experiments have supported this expectation [24].

## 2.2 Superconducting Radio Frequency Cavities

Linear particle accelerators are used at facilities such as the Continuous Electron Beam Accelerator Facility (CEBAF) at the Thomas Jefferson National Accelerator Facility (JLab) and the European Organization for Nuclear Research (CERN) accelerator complex. These linear accelerators (linacs) consist of resonator cavities that typically operate in the radio frequency regime. Superconducting radio frequency (SRF) cavities (e.g. niobium cavities) are preferred over normal conducting (e.g. copper cavities) because they are capable of higher quality factors, duty cycles, and

lower RF losses. The quality factor,  $Q$ , of a cavity is related to the energy stored in the cavity ( $U$ ) compared to the power dissipated ( $P_C$ ) by

$$Q = \omega \frac{U}{P_C}, \quad (2.14)$$

where

$$\begin{aligned} U &= \frac{1}{2} \mu_0 \int_V |H|^2 dv \\ P_C &= \frac{1}{2} \oint_S R_{surf} |H|^2 ds \end{aligned} \quad (2.15)$$

and  $\omega$  is the operating frequency. Extensive reviews of SRF physics and applications can be found in references [25] and [5].

Because the cavities are constructed from a superconducting material, the cavities must be cooled using liquid helium to maintain the temperature well below the material's  $T_C$ . A representative cross section of a typical cylindrically symmetric SRF cavity is shown in Figure 2.7. When a resonant electromagnetic mode is used to accelerate a charged particle, an alternating electric field is present along the direction of propagation. Because the electric field inside the cavity is alternating, there is also an associated magnetic field that travels parallel to the cavity surface. Since the magnitude of this magnetic field is proportional to the magnitude of the applied electric field for any electromagnetic wave, the ultimate accelerating gradient (related to the applied electric field) that can be achieved by an SRF cavity is limited by how much magnetic field the superconductor can withstand before vortex penetration decreases the efficiency of the cavity and/or quenches it altogether.

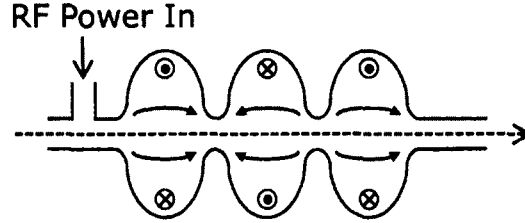


Figure 2.7: SRF cavity.

For many years, niobium has been the primary material used in SRF cavities due to its highest  $T_C$  (9.2 K) and  $H_{C1}$  (1700 Oe) values among the simple metals along with its ease of manufacturability. However, the use of niobium imposes a limit on the ultimate achievable accelerating gradient  $\sim 55$  MV/m, and individual cavities have already been fabricated that have operated near this limit [26] [27]. Once technology that operates at this limit is fully implemented in accelerator facilities, the only way to reach higher energy particle beams is to add more cavities or make more passes through existing cavities. One possible alternative to this option is to develop a new technology that implements materials other than niobium capable of achieving higher accelerating gradients. Since SRF is a surface phenomenon with magnetic fields penetrating less than  $1 \mu\text{m}$  into the surface, it presents the possibility of using thin film coatings to engineer the surface. In 2006, a model was proposed by Alexander Gurevich that uses a multilayer film coating to shield an underlying niobium cavity from higher magnetic fields, thus allowing for larger accelerating gradients [6]. This model is discussed in detail in the following section.

## 2.3 Potential Advantages of Thin Films

The Gurevich model involves using a multilayer thin film coating that consists of alternating superconducting-insulating-superconducting (SIS) layers that are deposited over thick niobium on a cavity's inner surface. As discussed earlier, magnetic fields will penetrate into the material and will decrease in magnitude according to Equation (2.4). There are two important aspects that are required for this model to be successful: decreasing the surface resistance and delaying vortex penetration.

In order to decrease the surface resistance and thus increase the efficiency or  $Q$  of the cavity, the superconductor in the multilayer coating must have both  $T_C > T_C^{Nb}$  and  $H_C > H_C^{Nb}$ , where  $H_C$  is the thermodynamic critical field corresponding to the field at which all the magnetic flux has entered the superconductor. A few candidate superconductors that fit this criteria include NbN, Nb<sub>3</sub>Sn, and MgB<sub>2</sub>.

For a superconducting thin film whose thickness is less than its London penetration depth and is in the presence of a magnetic field that is parallel to the film's surface, the film's effective  $H_{C1}$  value can be tailored according to

$$H_{C1} = \frac{2\phi_0}{\pi d^2} \ln \frac{d}{1.07\xi} \quad \text{for } d < \lambda, \quad (2.16)$$

(where  $d$  is film thickness) by changing the film's thickness [28]. As shown in Figure 2.8, this enhancement of  $H_{C1}$  can enable support of magnetic fields larger than  $H_{C1}^{Nb}$ . Successful shielding of a bulk niobium cavity can be achieved using superconducting films tailored to withstand larger magnetic fields than bulk niobium, along with

insulating layers to trap magnetic flux. This trapped magnetic flux will need to be canceled it before vortices can form in the opposite direction (remember that the electric and magnetic fields are alternating), as shown in Figure 2.9.

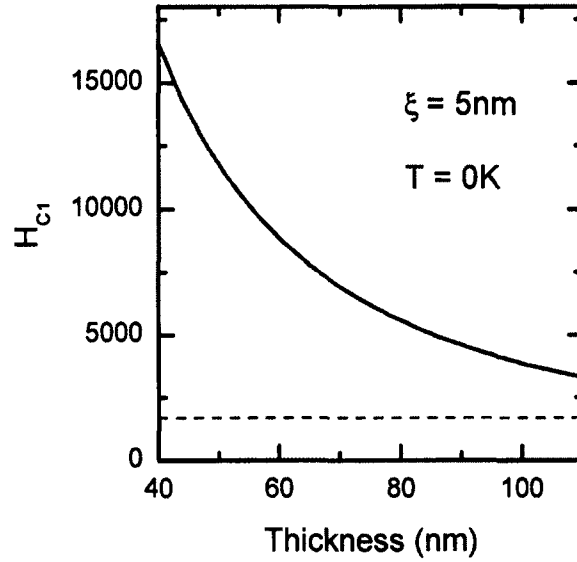


Figure 2.8: Enhancement of  $H_{C1}$  as a function of thickness for a thin film superconductor with a coherence length of 5 nm. The dashed line corresponds to  $H_{C1}^{Nb} = 1700$  Oe.

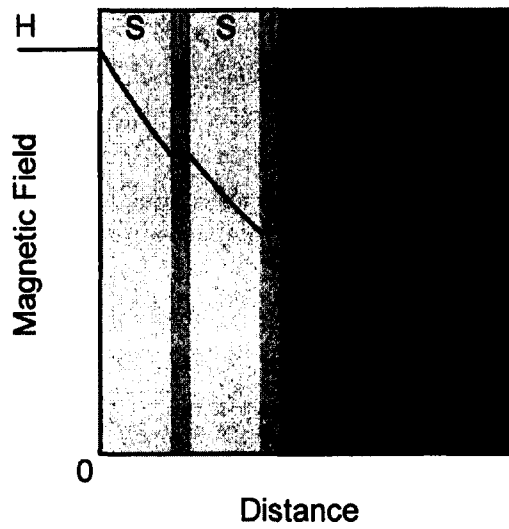


Figure 2.9: Illustration of how an SIS coating shields the bulk niobium cavity from higher magnetic fields, reducing the effective field experienced by the underlying surface.

The magnetic field at the interface,  $H_i$ , between the bulk niobium cavity and the SIS coating can be calculated using

$$H_i = H_0 e^{-\frac{Nd}{\lambda}}, \quad (2.17)$$

where  $H_0$  is the field at the surface,  $N$  is the number of superconducting layers with thickness  $d$  and London penetration depth  $\lambda$  found in the SIS coating. In principle, one can use this equation to determine how many superconducting layers of what thickness are necessary to shield the underlying cavity. Since material properties can be affected in thin film geometry as well as by the material's microstructure and surface/interface morphology, a systematic study on these effects on SRF behavior must be undertaken.

Gurevich's theoretical simulations show an increase in both Q and achievable magnetic field in coated cavities. A representative plot comparing a bare niobium cavity and a coated cavity is shown in Figure 2.10.

The first experimental evidence supporting Gurevich's model was presented by Antoine *et al.* who fabricated proof of principle NbN/MgO/Nb SIS structures [29] [30]. DC SQUID measurements and AC third harmonic analysis showed that the NbN film was successful in shielding the underlying niobium film. In both measurement techniques, the niobium film saw field penetration around 180 Oe while the SIS structure was able to delay field penetration up to 960 Oe. While evidence of shielding was presented, the maximum magnetic field that was applied before vortex entry was still

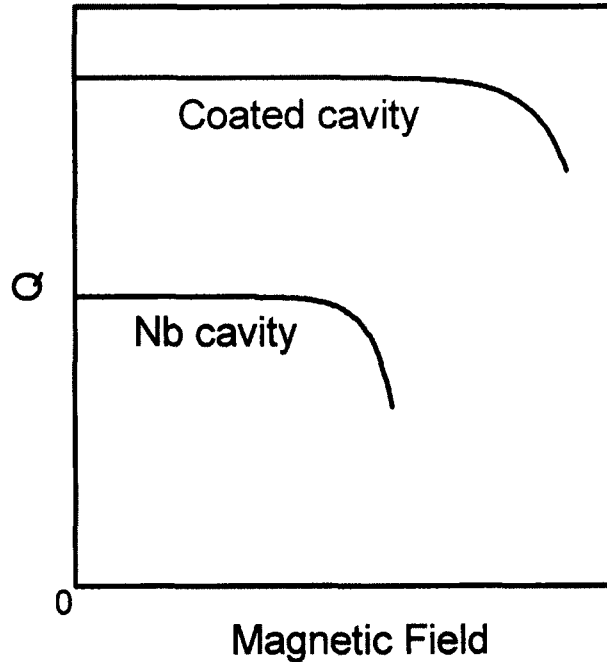


Figure 2.10: Representative plot of the theoretical improvement in  $Q$  and magnetic field for a bare versus coated cavity.

lower than  $H_{C1}$  of bulk niobium. Since this first evidence was presented, research has also been carried out on other niobium compounds such as NbTiN [31]. In addition to niobium based compounds, novel superconductors like  $MgB_2$  have received a great deal of attention due to its two energy gaps and high  $T_C$  around 39 K [32] [33] [34] [35] [36] [37].

In order to measure the RF properties of small samples, both bulk coupons as well as SIS structures, several measurement systems have been developed specifically for characterizing small samples. These systems include a disk resonator system [38], a surface impedance characterization system [39], and a quadrupole resonator system [40]. One advantage of characterizing the RF behavior of small samples is that



these samples can be characterized using a variety of methods that are not suitable for bulk cavities unless the a cavity is destroyed. For example, a small sample can have its surface morphology and microstructure studied using laboratory instruments where has a bulk cavity would need to be broken into smaller pieces in order to be characterized using these instruments. With the RF behavior correlated to properties of small samples such as surface morphology, microstructure, and DC transport properties, a better understanding of what are the important factors regarding RF performance can be obtained and used for successfully scaling up and implementing SIS technology.

## Chapter 3

# Fabrication and Characterization

The experimental methods used in preparation of the work described in this dissertation can be classified into two categories: sample fabrication and material characterization. The primary method of thin film deposition used in our research was DC sputter deposition. We note that this form of film deposition has been used for this application in the pioneer work carried out at CERN [41]. In this chapter, the physical processes and alternate modes of sputter deposition are discussed. Following the film growth description, the material characterization methods are discussed. These include structural and surface morphology characterization methods such as reflection high energy electron diffraction, atomic force microscopy, X-ray diffraction and reflectivity, as well as the characterization of superconducting properties using superconducting quantum interference device magnetometry.

## 3.1 Film Deposition

### 3.1.1 DC Magnetron Sputtering

Sputtering is a form of physical vapor deposition that is commonly used in thin film and multilayer deposition of large surfaces. A schematic showing the basic requirements for sputter deposition is shown in Figure 3.1. The sputter deposition process requires the deposition chamber to be pumped down to the lowest achievable pressure (typically in  $10^{-8}$  to  $10^{-10}$  Torr range) to provide the cleanest environment possible. A mechanical forepump is used to pump from atmosphere (760 Torr) down to the  $10^{-2}$  Torr range, followed by either a turbomolecular pump or cryogenic pump from the  $10^{-2}$  Torr range down to the system's base pressure.

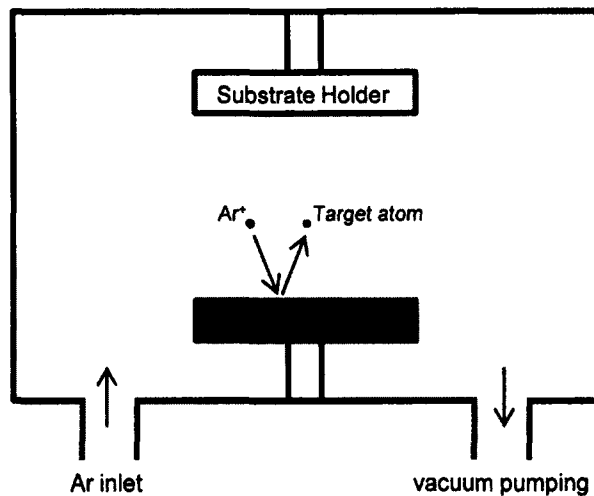


Figure 3.1: A typical setup for sputtering.

Once the system has been pumped down, it is then backfilled with 99.999% pure

Ar gas into the mTorr pressure range. A high negative potential is applied to the material that is to be deposited (the target material) to create a plasma such that Ar ions ( $\text{Ar}^+$ ) are attracted to the target. When a massive Ar atom collides with the target, the momentum from the Ar atom is transferred to a target atom that is subsequently ejected or sputtered from the target. In order to increase the efficiency of the sputtering process, magnetron sputtering sources are often used. Magnetron sources have magnetic fields located near the target that modify the electrons trajectory. Electrons traveling through the chamber that are trapped by these magnetic fields will move in a helical motion around the magnetic field which will increase the chance of ionizing an Ar atom near the target. The use of a magnetron source confines the plasma to a region near the target and increases the number of Ar ions, which leads to larger growth rates.

### **3.1.2 Reactive Sputtering**

DC voltages are sufficient for use with conducting targets but cannot be used with non-conducting target materials. To overcome this difficulty, radio frequency (RF) voltages can be used. Additionally, in some cases in order to deposit a compound film that is not a good conductor with a DC voltage, a reactive sputtering process can be used. Reactive sputtering involves introducing a reactive gas (in addition to the Ar) that can form a compound with the target material. Compounds can be formed using a metallic target and gases like oxygen or nitrogen to form oxides (e.g.  $\text{MgO}$ ) or nitrides (e.g.  $\text{NbN}$ ) respectively. Figure 3.2 shows a schematic of the

reactive sputtering process to create a nitride film. Because the reactive gas is located throughout the vacuum chamber, reactions can occur with the target, at the substrate, and also with the sputtered atoms in the gas phase (with a sufficiently high working pressure) [42]. The ratio of the reactive gas to Ar can change the composition and stoichiometry of the deposited film, which allows the film's properties to be tailored by tuning this ratio.

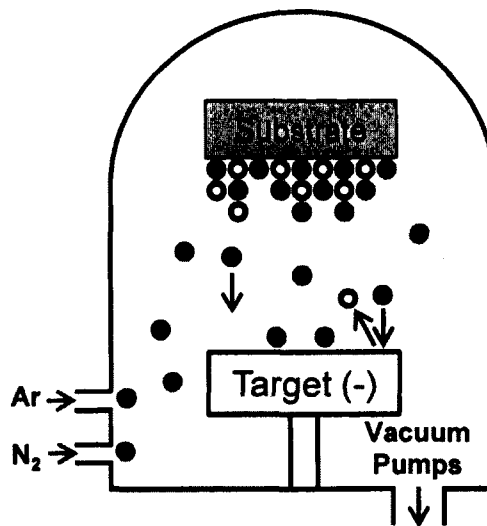


Figure 3.2: A typical setup for reactive sputtering.

Sputter deposition processes are often used in applications that require precise control of film properties, uniformity, and reproducibility [43] [44]. Applications that require multilayer deposition such as semiconductor devices and Josephson junctions often utilize sputter deposition. With the current status of sputtering technology and its broad usage across many disciplines, sputter deposition is a logical choice for depositing the multilayer structure required in Gurevich's SIS model.

While the exact specifications and tolerances for optimal performance have yet to be determined, there are several quantities that can have certain boundaries placed on them. For example, we know that the thickness of the superconductor in the SIS model must be less than its London penetration depth, which is generally a few tens or hundreds nanometers for the candidate materials. Additionally, the enhancement of  $H_{C1}$  calculated using (2.16) begins to see diminishing returns around 10 nm. This tells us that superconducting films on the order of tens of nanometers will be deposited in these SIS structures. The number of layers and the thickness of each layer required can be tuned to the magnitude of the magnetic field that is to be shielded using (2.17). Another difficulty in trying to determine the optimal thickness is that the model assumes bulk like properties and does not account for factors like strain that are present in thin films. The model also does not provide any guidance as to what is the optimal thickness for the insulating layer other than it must be sufficiently thick as to decouple the superconducting layers that it separates.

An acceptable tolerance has also not yet been determined for the surface roughness. As is the case with bulk cavities, a smoother surface will generally result in better performance by minimizing local field enhancements. An upper bound can be put on the roughness that corresponds to the thickness of the film that is to be deposited onto a surface. For example, if a surface (whether bulk or a series of deposited layers) has surface features that are 20 nm thick, a film that is 15 nm thick will not attain full coverage of the surface. This lack of full coverage would lead to voids and defects which would cause decreased performance. Other than stating smoother is

better and full coverage is required, no other bounds have been quantified. Again, from the standpoint of the model, smooth interfaces are assumed and therefore real surface features are not accounted for.

Gurevich provides one example SIS structure in his paper containing three layers of Nb<sub>3</sub>Sn that are 50 nm thick ( $\lambda_L = 65$  nm) and separated by insulating layers. This structure would attenuate an external magnetic field to 10% of its original magnitude by the time the field reaches the interface of the coating and the bulk cavity.

In addition to producing proof of principle samples, sputter deposition is also capable of coating SRF cavities. For example, one alternate mode of sputtering called High Power Impulse Magnetron Sputtering (HIPIMS) has been considered for depositing superconducting thin films onto SRF cavities [45]. This sputtering mode is a form of energetic condensation that can produce films that are more dense and smoother than alternative deposition methods [46]. In addition to considering HIPIMS for coating SRF cavities, other growth methods such as electron cyclotron resonance plasma [47], cathodic arc coaxial energetic deposition [48], and atomic layer deposition [49] are also being explored since they have shown promising results.

## **3.2 Film Characterization**

### **3.2.1 Reflection High Energy Electron Diffraction**

Reflection high energy electron diffraction (RHEED) is a technique that allows for *in situ* characterization of material surfaces. RHEED was first demonstrated in 1928

by Nishikawa and Kikuchi [50, 51]. This technique requires an electron source and a phosphor screen in order to characterize a sample's surface. The geometry required for RHEED is shown in Figure 3.3.

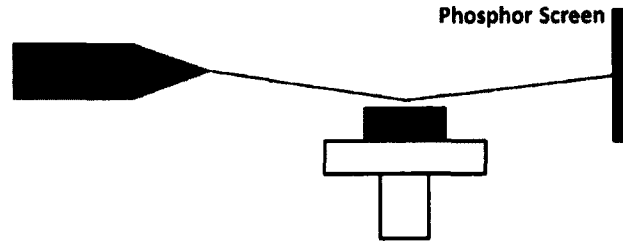


Figure 3.3: A typical setup for the RHEED geometry. In this geometry, an electron beam is incident on a sample's surface at a glancing angle of less than  $4^\circ$ .

RHEED is typically operated in HV-UHV environments, and therefore it is not adequate to monitor growth in real time using sputtering. Differential pumping can be implemented to use it in such cases. Conversely, it can be used after sputter deposition and/or during pre-and post-growth thermal treatments. The penetration depth of electrons in the sample is very short, and therefore the penetration depth of the RHEED beam is quite shallow. Thus, RHEED can obtain information regarding the structure of the few atomic planes closest to the surface. The sample being examined can also be rotated azimuthally such that various crystallographic directions can be examined. The wavelength of the incident electrons can be calculated using the de Broglie relationship

$$\lambda = \frac{h}{p} \quad (3.1)$$



where  $\lambda$  is the electron wavelength,  $h$  is Planck's constant, and  $p$  is the electron's momentum. By substituting in the relationship between kinetic energy and momentum,  $E = \frac{p^2}{2m}$ , and a typical value for an electron's energy in a RHEED system, we find the wavelength of the electron to be

$$\begin{aligned}\lambda &= \frac{h}{p} \\ \lambda &= \frac{hc}{\sqrt{2mc^2 E}} \\ \lambda &= \frac{1.239 \cdot 10^4 \text{ eV} \cdot \text{\AA}}{\sqrt{2(5.110 \cdot 10^5 \frac{\text{eV}}{c^2})(2.9 \cdot 10^4 \text{ eV})}} \\ \lambda &= 0.072 \text{\AA}.\end{aligned}\tag{3.2}$$

Due to this small wavelength, RHEED can probe the interatomic spacing in material surfaces. To understand where the resulting diffraction patterns come from, we must examine the materials in reciprocal space. A reciprocal lattice for a given structure can be found by computing a Fourier transform of a real lattice. For a three-dimensional crystal, its reciprocal lattice is a three-dimensional array of points. The conditions for allowed diffraction (and therefore a diffraction pattern on the RHEED screen) are met when the points in the reciprocal lattice are intersected by the Ewald sphere. The Ewald sphere is used to represent the interaction between an incident wave (such as an electron beam) and a reciprocal lattice. The radius of the Ewald sphere is given by

$$k_0 = \frac{2\pi}{\lambda}\tag{3.3}$$

where  $\lambda$  is the electron wavelength.

The intersections between the Ewald sphere and the reciprocal lattice for a three-dimensional material would occur only at certain points as shown in Figure 3.4 (a). A diffraction pattern from this interaction would consist of sharp spots correlating to each intersection. However, since the electrons in a RHEED measurement only penetrate a few surface layers, the crystal that the electron beam is incident on can be modeled as a two-dimensional crystal. The reciprocal lattice of a two-dimensional crystal is a series of rods of infinite length that are normal to the real surface. For this case, the intersections between the Ewald sphere and the lattice rods occurs over some distance along the rod as shown in Figure 3.4 (b). The diffraction pattern resulting from this interaction would consist of sharp streaks as opposed to single points. The distance between the streaks in the diffraction pattern are inversely proportional to the real space atomic distance that is being probed (i.e. smaller spacing between atoms will have a diffraction pattern with a larger distance between streaks and vice versa). Additionally, for a real surface the reciprocal lattice rods have a finite width due to defects, lattice imperfections, and thermal vibrations [52]. An increase in defects, such as smaller grains, would lead to wider streaks in the diffraction pattern. As surface roughness increases via the formation of three-dimensional features, the RHEED pattern will transition from streaks to a superposition of streaks and spots[53]. Chevron features will also appear superimposed onto the streaks if a crystalline surface forms faceted features that have specific angular orientation with respect to the surface normal [54][55]. For a crystalline material that has grains that are rotationally disorganized, the RHEED pattern will appear as rings. Figure 3.5

shows the expected RHEED patterns for a (a) three-dimensional material exhibiting a spotty pattern, (b) a high quality surface exhibiting a sharp streak pattern, (c) a lower quality surface with some degree of roughness exhibiting a spotty and wider streak pattern, and (d) a material with rotationally disorganized grains exhibiting a ring pattern. Experimentally acquired patterns for a high quality surface and a rotationally disorganized surface are shown in Figure 3.6 (a) and (b) respectively.

Because of RHEED's powerful ability to probe the crystallographic structure of surfaces *in situ*, it is commonly used to characterize thin films during and after deposition. It is commonly found in molecular beam epitaxy deposition systems where it can be used to monitor growth rates as well as crystal structure due to the lower operating pressure than other deposition methods. Further information and applications of RHEED can be found in references [56] and [57].

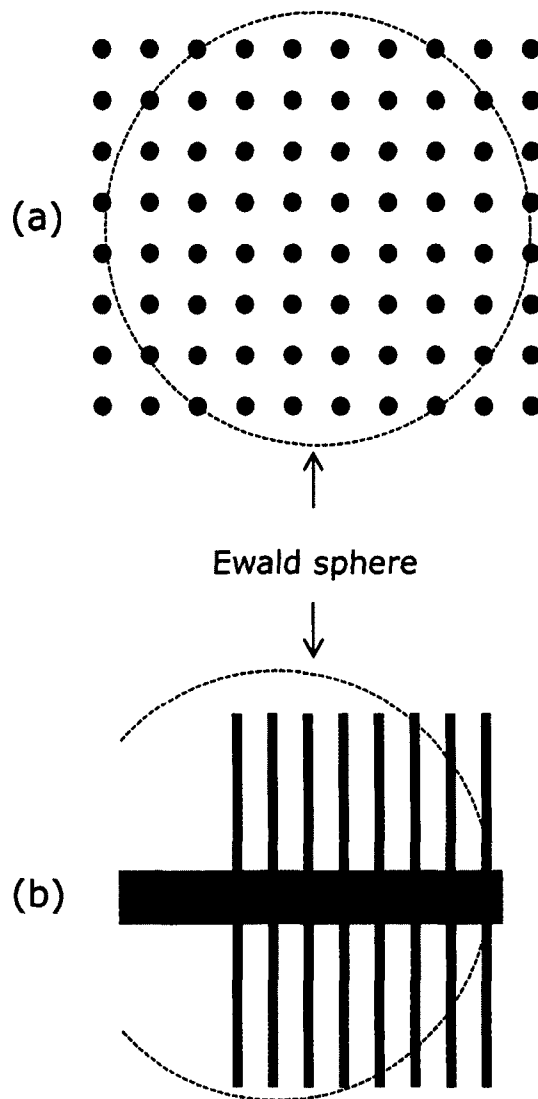


Figure 3.4: (a) Top down view of an Ewald sphere intersecting points in a reciprocal lattice for a three dimensional material. (b) Side view of an Ewald sphere intersecting reciprocal lattice rods which would result in a RHEED pattern containing streaks.

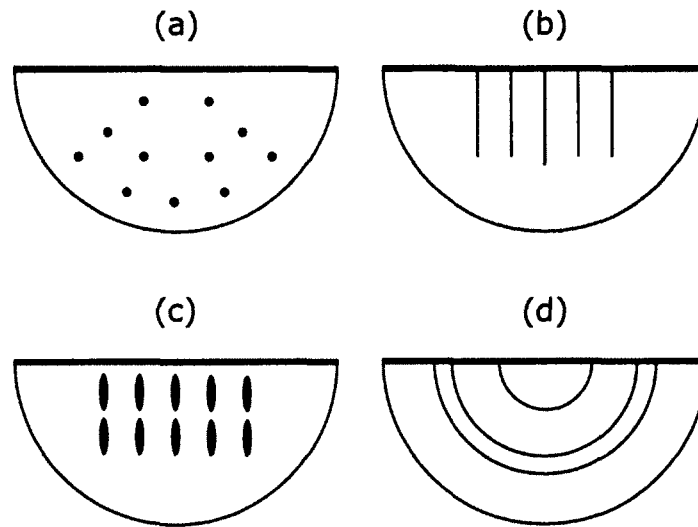


Figure 3.5: Expected RHEED patterns for (a) a three-dimensional material, (b) a high quality surface, (c) a lower quality rough surface, and (d) a surface with rotationally disorganized grains.

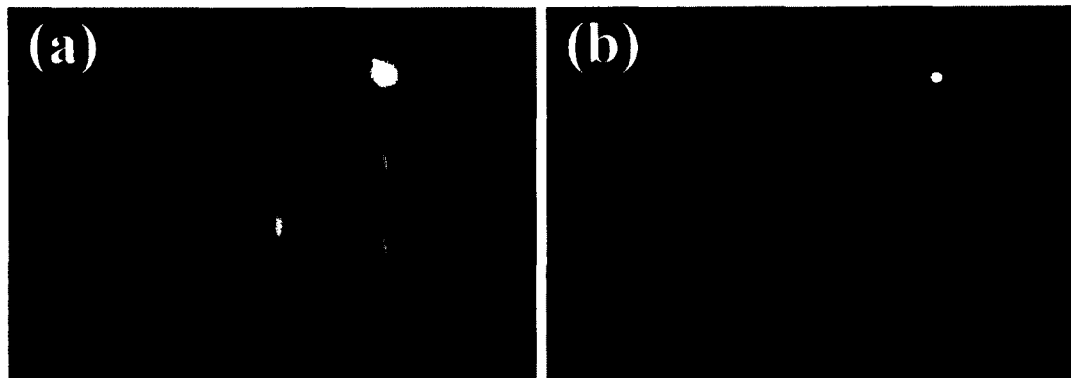


Figure 3.6: (a) RHEED pattern for a single crystal where the streak spacing indicates the atomic separation. (b) RHEED pattern for a material with crystallographic grains that are rotationally misaligned.

### 3.2.2 Atomic Force Microscopy

Scanning probe microscopy is a term used to describe many commonly used surface characterization techniques. All of these techniques can be traced back to the scanning tunneling microscope (STM) that was first demonstrated by Gerd Binnig and Heinrich Rohrer [58, 59]. The STM was able to achieve atomic resolution by rastering an extremely sharp tip over a surface in close enough proximity as to maintain a tunneling current between the tip and surface atoms. This method allows for surface properties, such as topography, as well as electronic properties, such as density of states, to be studied over very small areas.

Shortly after the invention of the STM, Gerd Binnig, Calvin Quate, and Christoph Gerber demonstrated a variant of the STM called the atomic force microscope (AFM) [60]. Instead of using a tunneling current, the AFM uses force interactions between the tip and sample to measure surface topography. These interactions can be monitored by using a tip with a reflective coating, such as aluminum, in conjunction with a laser and a photodiode detector as shown in Figure 3.7. When the AFM is operated in non-contact mode, the tip is oscillated at a driving frequency. As the tip approaches the surface, attractive forces such as van der Waals forces will cause a decrease in the oscillation amplitude. The feedback control system and the piezoelectric scanner use the amplitude decrease to control the tip-sample distance. In order to reduce the noise in acquired images that result from the surrounding environment, it is often necessary to implement acoustic isolation of the AFM through the use of an enclosure. Additionally, vibrational isolation can be achieved through active response tables or

spring-mass-damper platforms.

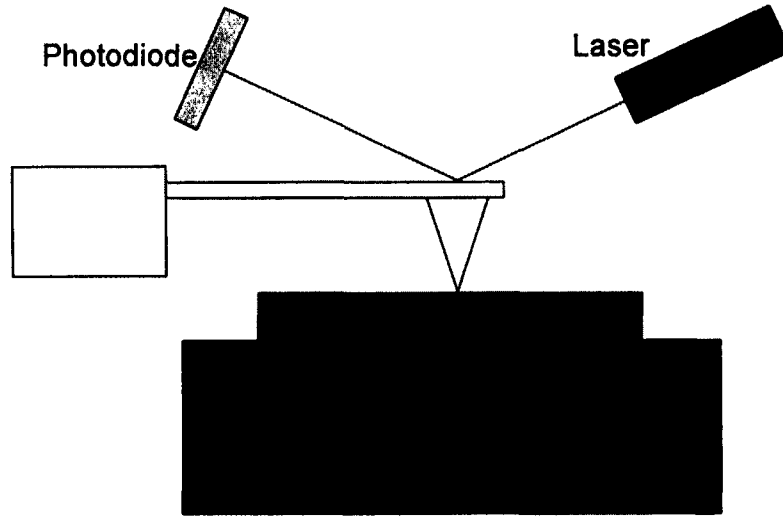


Figure 3.7: Schematic of an AFM setup.

For the work presented here, AFM images were acquired and analyzed using the WSxM (Windows Scanning  $x =$  Force, Tunneling, ... Microscope) software package developed by Nanotec Electronica [61]. This software enables useful topographic analysis such as the root mean square (RMS) roughness. The RMS roughness value is determined by creating a histogram of the height values in an image, fitting a Gaussian curve to the histogram, and using the standard deviation of this Gaussian as the RMS roughness. Additional frequency domain information can be obtained using fast Fourier transforms (FFT). Further analysis such as wavelength selection can be determined using power spectral density (PSD) on FFT images. An example process of obtaining PSD information is shown in Figure 3.8.

Recently, PSD analysis methods have been developed with the specific application

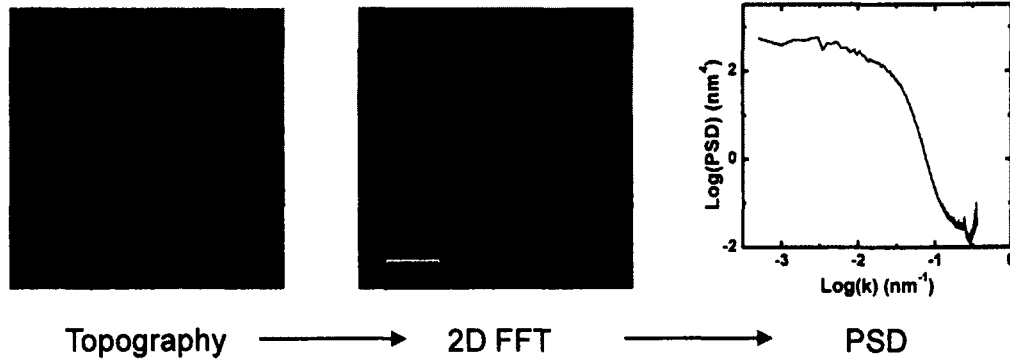


Figure 3.8: Starting from a topography image, a two dimensional FFT is calculated. From this 2D FFT, the PSD is calculated as a function of spatial frequency,  $k$ .

of SRF cavity surfaces in mind [62] [63]. Because PSD analysis is capable of providing more information than simple roughness analysis, these methods can provide useful insight into various processes used in SRF cavity fabrication. For example, bulk niobium cavities often go through either a buffered chemical polish or an electropolish in order to treat the surface before use. PSD analysis has provided scale specific information that will help provide more useful feedback with regards to how a certain polish process or recipe alters the surface morphology [64]. Ultimately, these methods will help determine the specific mechanisms that affect surface morphology providing useful information to optimize future processing of surfaces for SRF applications.

### 3.2.3 X-ray Diffraction

X-ray diffraction (XRD) is a characterization technique that probes the crystallographic structure of a material. In a crystalline material where the atoms are arranged in a periodic manner, X-rays can scatter and lead to both constructive and destructive



interference. Constructive interference can be used to determine inter atomic spacing provided that certain conditions are met. Figure 3.9 provides a simple schematic for these conditions.

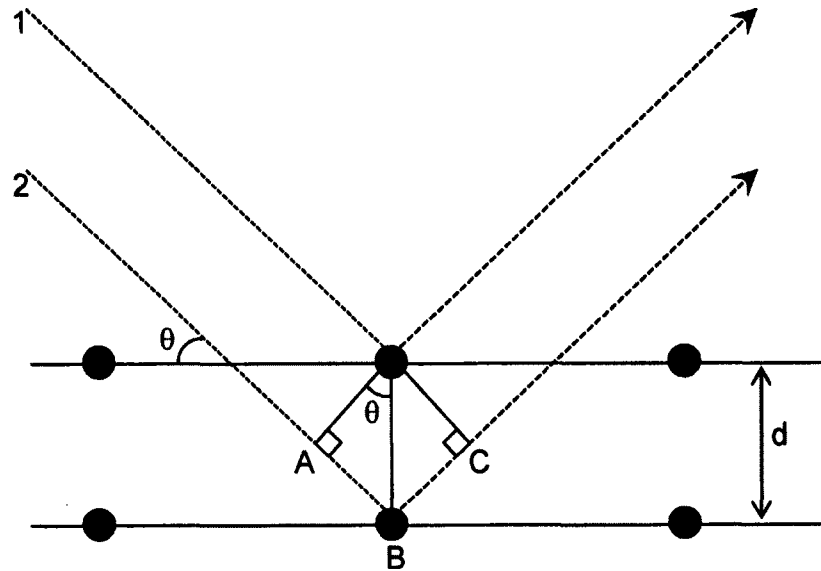


Figure 3.9: Constructive interference of two X-rays with atomic planes.

In order for X-ray 1 and 2 to remain in phase (and therefore provide constructive interference), the extra distance that X-ray 2 travels must equal an integer number,  $n$ , of X-ray wavelengths,  $\lambda$ , or

$$n\lambda = AB + BC. \quad (3.4)$$

Since  $AB = BC$ , we can simplify this to

$$n\lambda = 2AB. \quad (3.5)$$

Because the inter atomic distance,  $d$ , is the hypotenuse for the triangle formed by point A, point B, and the atom that scatters X-ray 1, we can relate  $d$  and  $\theta$  by

$$d \sin \theta = AB. \quad (3.6)$$

By substituting (3.6) into (3.5), we arrive at

$$n\lambda = 2d \sin \theta. \quad (3.7)$$

This equation was developed by William Lawrence Bragg [65] and is commonly referred to as Bragg's law. It should be noted that (3.7) is only valid for  $\lambda \leq 2d$ , thus requiring the short wavelengths found in X-rays in order to probe the subnanometer lattice spacing.

Typical laboratory XRD instruments generate X-rays by bombarding a target (such as Cu or Mo) with electrons whose kinetic energy are sufficient to knock out core shell electrons. When electrons from an outer shell drop to the core shell to fill the vacancy, an X-ray is emitted. For example, the Cu  $K\alpha$  transition (an electron knocked of the  $K$  shell is replaced by an electron from the  $L$  shell) produces X-rays with a wavelength of 1.54 Å.

A typical XRD scan ( $\theta - 2\theta$  scan) measures the intensity of diffracted X-rays as a function of  $2\theta$ . A peak in intensity around a given angle indicates that there are atoms arranged in a periodicity that can be calculated using (3.7). One disadvantage of plotting intensity as a function of  $2\theta$  is that the position of an identical lattice

spacing will shift depending on what X-ray wavelength is used. For example, a lattice spacing of 1.66 Å would produce a peak at  $2\theta = 55.64^\circ$  for a Cu  $K\alpha$  X-ray, but would have a peak at  $2\theta = 24.85^\circ$  for a Mo  $K\alpha$  X-ray. Therefore, unless the same X-ray wavelength is used, it can be tedious to compare XRD scans to previous experiments or literature references. However, if the intensity is plotted as a function of  $q_z$  the wavelength dependence is removed. This  $q_z$  notation is commonly used for experiments carried out at tunable wavelength facilities such as synchrotrons. To convert from a  $2\theta$  axis to a  $q_z$  axis, we first rearrange (3.7), solving for  $d$  to find

$$d = \frac{n\lambda}{2 \sin \theta}. \quad (3.8)$$

To represent the lattice spacing in reciprocal space, we use

$$q_z = \frac{2\pi}{d}, \quad (3.9)$$

which can be rearranged to

$$d = \frac{2\pi}{q_z}. \quad (3.10)$$

By setting (3.8) and (3.10) equal, we find

$$\frac{n\lambda}{2 \sin \theta} = \frac{2\pi}{q_z}. \quad (3.11)$$

Solving for  $q_z$ , we arrive at

$$q_z = \frac{4\pi \sin \theta}{n\lambda}. \quad (3.12)$$

Once we convert  $2\theta$  values to  $q_z$ , peaks representing  $1.66 \text{ \AA}$  for both the Cu  $K\alpha$  and Mo  $K\alpha$  X-ray wavelengths would appear at  $q_z = 3.81 \text{ \AA}^{-1}$ .

In addition to lattice spacing, additional information such as average crystallographic grain size can be obtained from these scans. In 1918, Paul Scherrer developed an equation that describes how the width of diffraction peaks increases as the average grain size decreases [66]. The Scherrer equation is given as

$$L = \frac{k\lambda}{B \cos \theta}, \quad (3.13)$$

where  $L$  is the average grain size,  $k$  is the shape factor (0.94 for cubic crystals),  $B$  is the full width at half max of the diffraction peak, and  $\theta$  is the Bragg angle where the peak occurs. Ultimately, the Scherrer equation gives a lower limit for the grain size since other factors such as strain, or instrumental effects can result in further peak broadening. Because the X-rays are probing the entire sample and are typically sampling multiple grains, the calculated grain size represents an average of all grains within the probed region.

A standard diffractometer with the capability of changing only the angles of the incident X-rays and detector (along the  $\theta - 2\theta$  circle) is sufficient for bulk materials and powders, but a special four circle goniometer is needed to characterize thin film samples since films may not be exactly parallel to the substrate where they were

deposited within the diffractometer resolution. Thus, optimization of the sample's alignment with respect to the actual film is mandatory so that the data is not overwhelmed by the substrate signals. A four circle goniometer, or an Eulerian cradle, has additional degrees of rotation for the sample as shown in Figure 3.10. The  $\phi$  circle allows for azimuthal rotation about the axis normal to the surface of the sample. The  $\omega$  circle allows the sample to rotate along the  $\theta - 2\theta$  circle, but independent of the incident beam and detector motion. The  $\chi$  or  $\psi$  circle allows the sample to rotate along the axis that is orthogonal to axes about which the  $\omega$  and  $\phi$  circles rotate. Because of the smaller amount of material in thin films and the possible misalignment with respect to the substrate, these additional circles are required to properly align the X-ray beam and detector with the actual thin film.

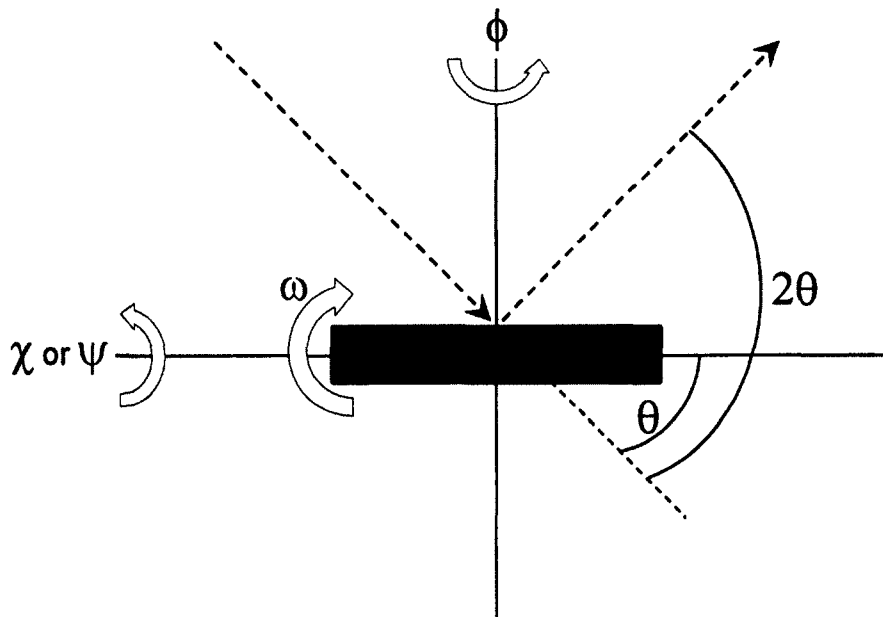


Figure 3.10: Four circle diffractometer.

In real crystals, all of the atoms will not be perfectly arranged on a lattice. Instead, there will be small regions or grains in which the atoms are arranged on a lattice. As shown in Figure 3.11, there can be a small misalignment between the individual grains which leads to what is called a mosaic structure. The degree of mosaicity in a crystal can be easily determined using XRD using what is called a rocking curve. To perform a rocking curve, the incident X-ray beam and detector are fixed in position while the sample is rotated or “rocked” about the  $\omega$  circle. The intensity vs.  $\omega$  plot will typically have a Gaussian shape where the width represents the degree of mosaicity.

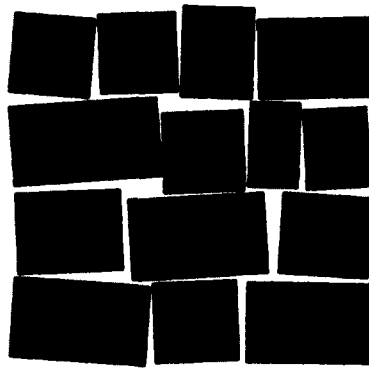


Figure 3.11: Simplified representation of mosaic structure typically found in crystalline materials.

Rocking curves can also be used to determine the offset or misalignment of a thin film with respect to a substrate. To do so, a rocking curve and subsequent  $\theta - 2\theta$  scan must be performed optimized for both the film and the substrate. The individual offset for each optimization is the difference between the optimized  $\omega$  value (center of rocking curve) and the Bragg angle such that

$$\text{Offset}_{\text{film}} = \omega_{\text{film}} - \theta_{\text{film}} \quad (3.14)$$

$$\text{Offset}_{\text{substrate}} = \omega_{\text{substrate}} - \theta_{\text{substrate}}. \quad (3.15)$$

The misalignment between the film and the substrate is simply the difference of the individual offsets

$$\begin{aligned} \text{Offset}_{\text{difference}} &= \text{Offset}_{\text{film}} - \text{Offset}_{\text{substrate}} \\ \text{Offset}_{\text{difference}} &= (\omega_{\text{film}} - \theta_{\text{film}}) - (\omega_{\text{substrate}} - \theta_{\text{substrate}}). \end{aligned} \quad (3.16)$$

Additional crystallographic information such as epitaxial relationship and in-plane spacing can be obtained using asymmetric ( $\chi \neq 0^\circ$ ) scans. For example, let us examine a (100) oriented cubic film deposited onto a (100) oriented cubic substrate (this information can be obtained using symmetric  $\theta - 2\theta$  scans). If we set  $\chi \approx 45^\circ$ , spacing between the (110) planes can be obtained. With the knowledge of the out of plane lattice parameter ( $\theta - 2\theta$  scan) and the spacing along the diagonal (asymmetric scan), the in-plane lattice parameter can be calculated using simple geometry. While the alignment is optimized for the film, a scan about the  $\phi$  axis should reveal four peaks separated by  $90^\circ$  due to the cubic structure. The  $\phi$  scan is then repeated optimized for the substrate, again showing four peaks separated by  $90^\circ$ . We can now compare the  $\phi$  scans of the film and substrate to determine the full epitaxial relationship. If the peaks from the film and substrate are aligned, then the film grew

in the (100)[001]|||(100)[001] orientation. If the peaks are offset by 45° between the film and the substrate, then the film grew in the (100)[110]|||(100)[001] orientation.

### 3.2.4 X-ray Reflectivity

X-ray reflectivity (XRR) is another powerful tool that uses glancing X-rays to probe information about thin films including thickness, roughness, and density. When X-rays encounter an interface, some will be transmitted and some will be reflected. For a perfectly flat interface between two materials with differing indices of refraction, the transmission and reflection can be modeled using the Fresnel equations. For an interface with a degree of roughness, there will be deviations from the Fresnel equations. XRR involves measuring the intensity of reflected X-rays as a function of glancing angle (typically less than 8°). A typical XRR scan is shown in Figure 3.12. Once the incident angle overpasses the angle of total internal reflection or critical angle (related to the material's density), the reflected intensity will decrease rapidly. The overall slope of the decrease is related to the surface/interface roughness. In addition to the overall decrease, a series of fringes or oscillations also appears where the periodicity is related to film's thickness. The data obtained is typically fitted using a recursive algorithm developed by Lyman Parratt [67] to assign numerical values to the density, roughness, and thickness. It should be noted that XRR can also be used to characterize multilayer films.



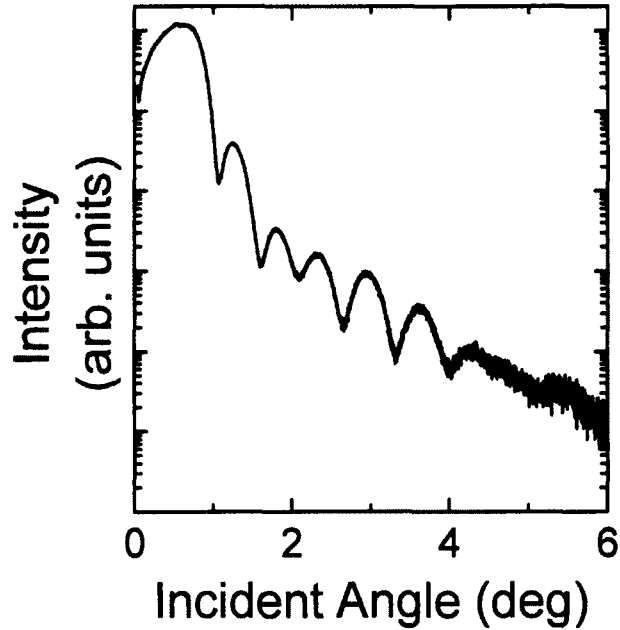


Figure 3.12: Typical XRR curve showing intensity oscillations.

### 3.2.5 SQUID Magnetometry

In order to measure the magnetic and superconducting properties of thin films, a superconducting quantum interference device (SQUID) magnetometer was used (specifically, the Quantum Design Magnetic Property Measurement System (MPMS)) [68]. The MPMS is capable of measuring the magnetic moment of a small samples (typically  $5 \text{ mm} \times 10 \text{ mm} \times 1 \text{ mm}$ ) as a function of temperature and applied field using a second derivative coil as shown in Figure 3.13 (a). This coil, constructed from superconducting wires, contains four coils with the outer two coils oriented in one direction and the inner two coils oriented in the opposite direction. Several centimeters away from the coil, the wires are connected directly to the SQUID. A SQUID is a tool that takes advantage of the Josephson effect that was first predicted by Brian Joseph-

son in 1962 [69] and experimentally observed by Philip Anderson and John Rowell in 1963 [70]. The Josephson effect is observed when two superconductors are separated by another material, such as an insulator, in a geometry called a Josephson junction, but are coupled by a supercurrent tunneling through the separating material. SQUIDs have a Josephson junction installed in the current loop that is connected to the detection coil which will act as a current to voltage converter. Provided that the sample size is sufficiently smaller than the detection coil, the output voltage can be modeled as the movement of a point-source dipole moving through the coil and using standard fitting algorithms is used to determine the magnetic moment of a sample. A typical output signal is seen in 3.13 (b).

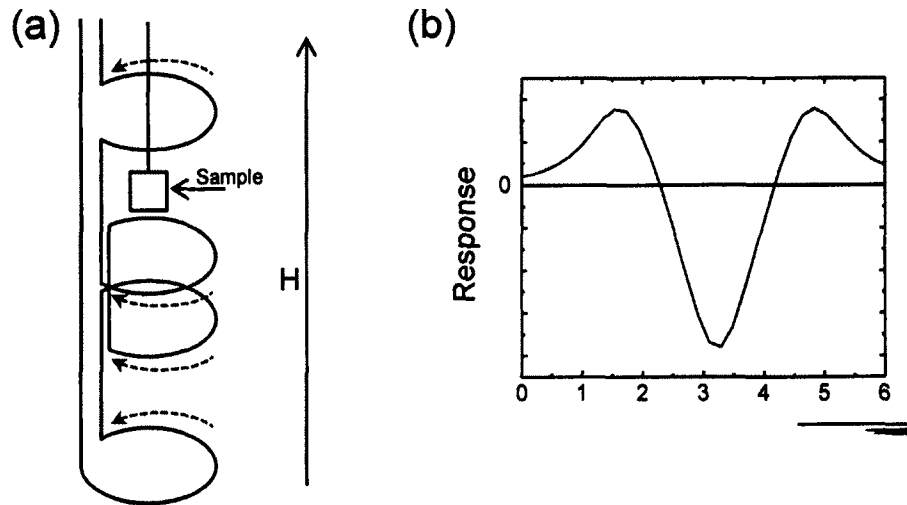


Figure 3.13: (a) The SQUID coil geometry showing the four detection coils, the sample, and the applied field. The directions of the arrows shows how the inner coils are oriented in one direction and the outer coils are oriented in the opposite direction. (b) A representative response curve showing the measurement from the four detection coils.

The MPMS is a useful tool because it can be used to measure superconducting properties such as  $T_C$  and  $H_{C1}$ . In order to measure  $T_C$ , the sample first undergoes a zero field cool (ZFC) to a temperature well below the expected  $T_C$  value. Next, a small magnetic field ( $H \sim 10-100$  Oe) is applied to obtain a diamagnetic response since the sample is in the Meissner state. The temperature is then increased until the sample's magnetic moment has decreased to zero, indicating that the sample has returned to the normal state. The temperature at which the moment reaches zero is taken to be  $T_C$ .

In order to measure  $H_{C1}$ , two different procedures were used and compared. The first and simplest method involves isothermal ramping of the applied field. That is, the sample is cooled down below  $T_C$  and the temperature is fixed. Next, the moment is measured as the applied field increases to achieve a curve similar to that found in Figure 2.5. However, in cases where flux pinning occurs,  $H_{C1}$  does not occur at the peak moment, but instead occurs at the first deviation from the Meissner slope. When flux pinning occurs and the magnetization is not reversible, a procedure developed by Böhmer *et al.* is implemented [71].

This procedure accurately determines  $H_{C1}$  by measuring trapped magnetic moments that appear after the application and removal of an applied field. The first step in this procedure is to do a ZFC into the superconducting state. The sample's magnetic moment is then measured. An external magnetic field is then applied and subsequently removed. The sample's magnetic moment is measured once again. The sample's magnetic moment before the application of the field is subtracted from the

moment after the removal of the field. The sample is then warmed up into the normal state and the procedure is repeated for several field values. The field at which there is a difference in the two magnetic moments indicates that there has been field penetration and thus this field is determined to be  $H_{C1}$ .

It should be noted that any misalignment between a film's surface and the direction of the applied field will lead to a decreased value for the measured critical field. Therefore, even when samples are aligned as well as experimentally possible, the measured field value will represent an underestimate or lower limit since the perpendicular component of the applied field would promote earlier vortex penetration. The magnetic moment of a thin film can be determined by

$$m = \frac{VH}{4\pi} \left( \cos^2 \theta + \frac{1}{1-D} \sin^2 \theta \right) \quad (3.17)$$

where  $m$  is the magnetic moment,  $V$  is the sample volume,  $H$  is the applied field,  $\theta$  is the angle between the applied field and the film's surface, and  $D$  is the demagnetization factor. The optimal alignment is achieved when  $m$  is minimized by achieving  $\theta = 0$  (and therefore  $1 - D = 0$ ). For the measurements presented in this dissertation, the sample mounting was adjusted such that a minimum moment was achieved, thus aligning the sample surface as parallel as possible with the applied magnetic field.

SQUID measurements also suffer from edge effects that will not be present in SRF cavities because the magnetic fields in an SRF cavity will always be parallel to the surface of the material. During SQUID measurements with the field oriented parallel

to the surface, the applied magnetic field will also interact with the edge of the sample (causing a perpendicular contribution) and potentially the backside or bottom of the film at the interface with the substrate depending on the magnetic behavior of the substrate used.

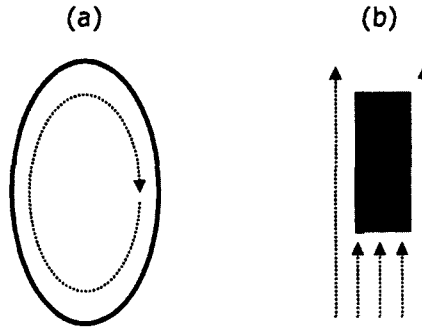


Figure 3.14: Magnetic field lines (represented as dashed lines) for (a) an SRF cavity operated in a typical  $TM_{010}$  mode and (b) a thin film mounted in a SQUID magnetometer.

When Antoine *et al.* witnessed shielding of niobium in a multilayer structure in their DC SQUID measurements, they explored how the edge effects would contribute to the overall behavior of the multilayer [29] [30]. In addition to DC SQUID measurements, they also measured the superconducting properties of their samples using an AC third harmonic analysis technique as demonstrated in references [72] [73] [74]. Because this measurement technique utilizes a local probe that is much smaller than the sample size, edge effects will not alter the results. Additionally, this technique probed the sample only from the side that was coated with NbN, therefore replicating an SRF cavity where the niobium will only see a magnetic field that has been attenuated by the SIS coating. When the DC and AC measurements were

compared, the results were very consistent with each other. Thus, DC SQUID measurements can be considered an accurate representation of the sample's behavior since results have been reproduced using an alternate technique that avoids issues like edge effects, which makes us confident regarding our approach to measure magnetic field shielding on our thin films and multilayered samples.

## Chapter 4

# Superconducting Thin Films and Multilayers

In our work towards developing an understanding of superconducting thin films and multilayers for the specific application of SRF accelerator cavities, we employed the techniques described in the previous chapter to correlate the surface morphology, microstructure, and superconducting properties in proof of principle samples testing the Gurevich model. As a result of this work, we have demonstrated that grain boundaries can have detrimental effects on superconducting properties [75], interfacial strain can lead to system losses in ultrathin films [76], NbN films have properties that make them a desirable candidate for SIS coatings [77], and that it is possible to delay vortex penetration beyond the lower critical field of niobium [78]. The following sections provide a detailed description of each of these studies.

## 4.1 Niobium Thin Films on Copper Surfaces

As stated in the introduction, because of the very shallow penetration depth of the RF fields, SRF properties are inherently a surface phenomenon, involving a material thickness of less than  $1\ \mu\text{m}$ . This fact opens up the possibility of using combinations of superconducting materials in thin film coatings. One can envision depositing a thin layer of niobium onto the inner surface of a castable cavity structure made of copper or aluminum as already demonstrated by the pioneer work carried out at CERN. This opens the possibility of dramatically changing the cost framework of SRF accelerators by decoupling the active SRF surface from the accelerating structure definition and cooling, while also combining different layers of materials with improved superconducting properties.

Thus, the use of thin films has the possibility of increasing thermal efficiency by exploiting the better thermal conductivity of copper or aluminum as compared to niobium. There have been several attempts of implementing niobium coated copper cavities with varying degrees of success [1]. It was mentioned already that material factors exist that can lead to diminished SRF performance compared to an ideal cavity. Factors such as intragranular impurities can contribute to reduced mean free path and  $H_{C1}$  values. Grain boundaries can also act as scattering centers as well sites that promote localization of impurities and lossy oxidation. These impurities and oxides found at grain boundaries contribute weak links to surface supercurrent flow leading to a nonlinear loss mechanism [79]. For thin films, additional factors such as



surface roughness, microstructure, and thickness (scattering due to the film/substrate interface is more prominent as the thickness decreases) can also affect superconducting properties. While it is a nontrivial process to identify the individual contributions from all of these factors, it is necessary to attempt understanding how they will change the superconducting properties so that thin film materials can be tailored to optimize SRF performance.

As a first step toward understanding the effect of these factors (in particular the surface morphology and grain boundary density), niobium films were deposited onto MgO(100) single crystal substrates so that they could be studied in an ideal scenario before being studied on more realistic surfaces. The films were deposited using DC sputtering using a 99.95% pure niobium target at a working pressure of 1 mTorr Ar with thicknesses varying from 100-1000 nm. Before deposition, the substrates were annealed at 600 °C for one hour to remove any residual contaminants (such as water) from the surface and to promote surface recrystallization, providing a high quality surface for subsequent deposition.

This choice of substrate was guided by the possibility of epitaxial growth leading to high quality films with regards to microstructure. Epitaxial growth occurs when a material that is deposited onto a crystalline substrate mimics the crystalline structure of the underlying surface. In the case where the film and substrate are different materials, this is referred to as heteroepitaxy. Because epitaxial films try to replicate the crystalline nature of the substrate, whether it is atomic spacing, crystallographic orientation, or crystallographic structure, there is a greater degree of order

in these films leading to fewer defects as compared to non-epitaxial polycrystalline films. For applications where defects are problematic, such as superconducting thin films, epitaxial growth is desired.

When niobium is deposited onto MgO(100) surfaces, two epitaxial relationships are possible:

Nb(100) with one inplane orientation

$$Nb(100)[011] \parallel MgO(100)[001]$$

and Nb(110) with two inplane orientation (4.1)

$$Nb(110)[\bar{1}\bar{1}0] \parallel MgO(100)[001]$$

$$Nb(110)[001] \parallel MgO(100)[001]$$

depending on the growth conditions and surface preparation [80]. A visual depiction of these orientations is shown Figure 4.1. For the case of Nb(100)/MgO(100) growth, the niobium lattice is rotated by 45° resulting in a 10.8% strain along the Nb[100] direction. For the Nb(110)/MgO(100) growth, there is anisotropic strain of 10.8% along the Nb[110] direction and 21.6% along the Nb[100] direction. Because both of these growth orientations are possible despite the Nb(110)/MgO(100) growth having a larger amount of strain, this indicates that other factors such as the substrate surface quality will help determine which orientation results after growth. In both orientations, niobium is deposited onto a substrate that helps it form its native cubic structure with some degree of strain at the interface that will progressively relax as the distance from the interface increases.

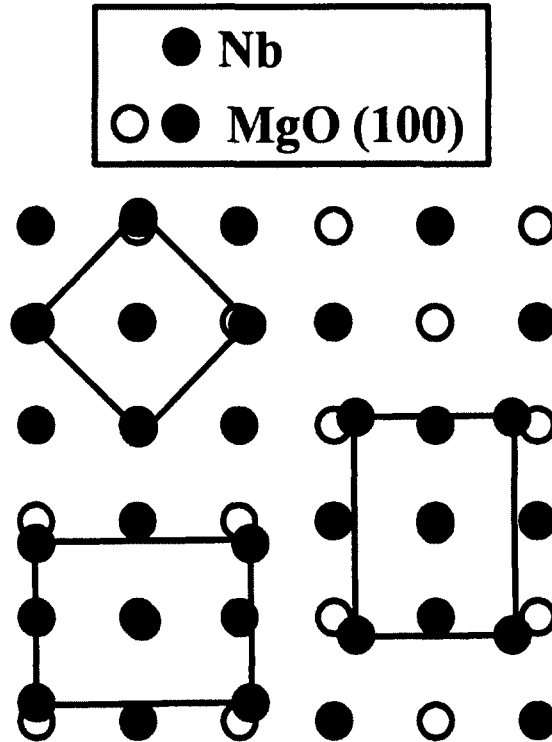


Figure 4.1: Overlays of relaxed niobium lattices on an MgO(100) surface.

Knowing the orientation of niobium with respect to the the MgO(100) substrate, we can determine what the expected RHEED patterns will look like as shown in Figure 4.2. In Figure 4.2 (a) the diffraction conditions are met such that RHEED is probing the Nb[100] distance resulting in a streak spacing that is inversely proportional to the lattice parameter,  $a$ . In Figure 4.2 (b), RHEED is probing the Nb[110] direction leading to a streak spacing that is inversely proportional to  $\sqrt{2}a$ . For the case of Nb(100)/MgO(100) growth, the Nb[100] direction would be found along the MgO[110] direction and the Nb[110] along the MgO[100] direction. Figure 4.2 (c) shows what would be seen along the MgO[100] direction for Nb(110)/MgO(100) growth with the coexistence of two orthogonal grains where RHEED can probe both  $a$  and  $\sqrt{2}a$

simultaneously.

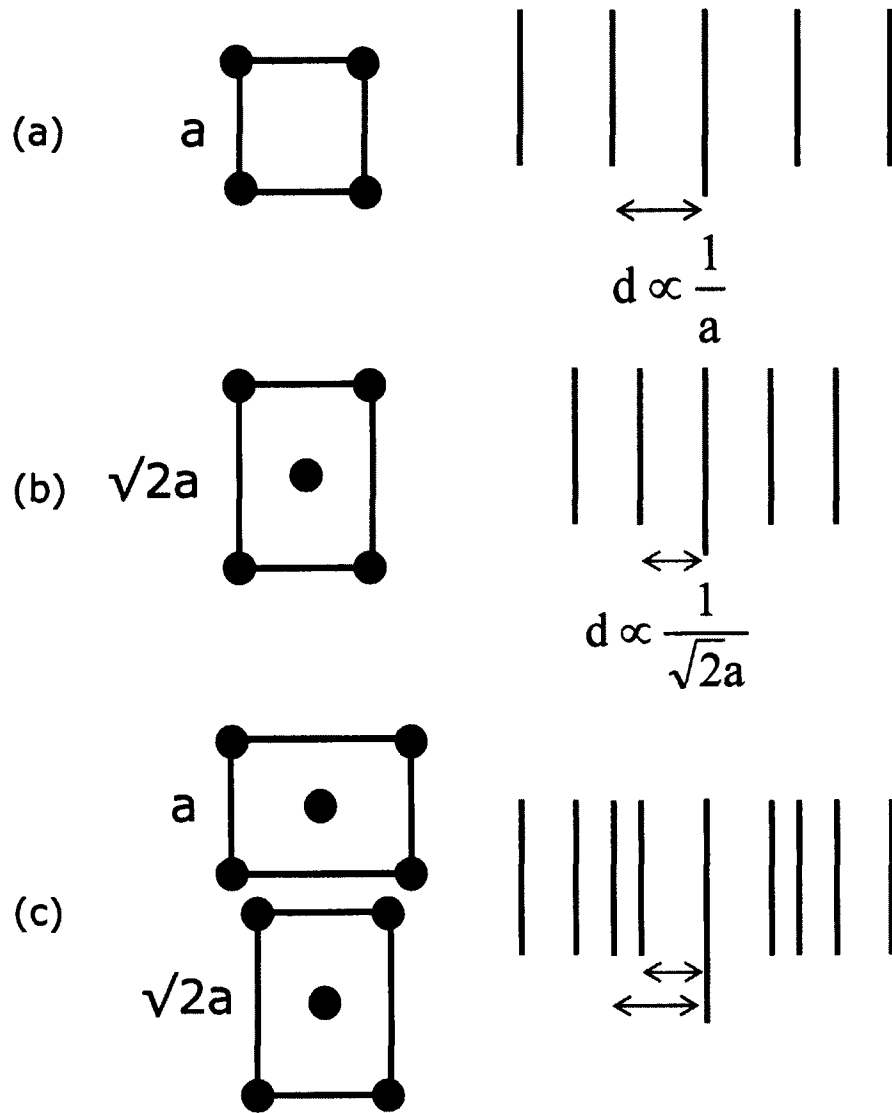


Figure 4.2: The expected RHEED patterns when the diffraction conditions are met for probing (a) the spacing along the Nb[100] direction, (b) the spacing along a Nb[110] direction, and (c) the distance along a Nb[100] and Nb[110] direction resulting from the coexistence of two orthogonal Nb(110) lattices.

The RHEED patterns acquired post deposition agree well with the possible epitaxial orientations as shown in Figure 4.3.

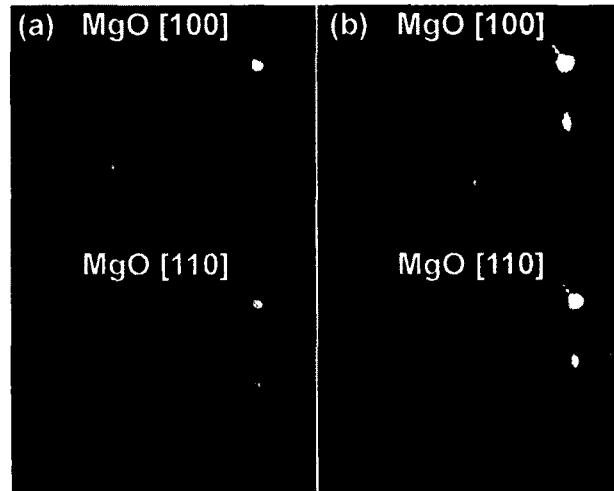


Figure 4.3: Typical RHEED patterns along the MgO[100] and MgO[110] azimuths for (a) Nb(100)/MgO(100) and (b) Nb(110)/MgO(100) surfaces.

Figure 4.3 (a) shows uniformly spaced streaks along two different azimuthal directions. The sharpness of the streaks is indicative of good crystal quality and large grain sizes. The spacing of the streaks in Figure 4.3 (a) (top) correspond to a Nb<110> spacing while the spacing in 4.3 (a) (bottom) correspond to the Nb<100> spacing. The chevron features along the MgO[100] direction correlate to the presence of faceted features. These observed patterns agree well with previously reported RHEED patterns of Nb/MgO growth [80] [81] [82].

The streaks found in Figure 4.3 (b) are also sharp, indicating good crystal quality, but a superposition of two spacings is present as opposed to one spacing as previously discussed. This observation is in agreement with the earlier discussion of the Nb(110)/MgO(100) epitaxy where two different in plane orientations are possi-

ble. Additionally, the pattern seen along the MgO[110] direction is consistent with patterns that have been seen in other Nb(110) growth systems [83].

XRD measurements were carried out to study the out of plane lattice spacing as well as average grain size. For all of the niobium films thicker than 500 nm, the out of plane lattice parameter was less than 1% strained as compared to the bulk value of 3.300 Å. While there was no significant difference between the lattice parameter in the Nb(100) and Nb(110) films, the Nb(100) films consistently had larger average grain sizes that ranged from  $52 \pm 2$  nm to  $86 \pm 3$  while the Nb(110) films had an average grain size around  $44 \pm 2$  nm. The larger grains found in the (100) films is indicative of coalescence during growth, thus minimizing grain boundary density through a process called Ostwald ripening [84]. Because the (100) films have larger grains, and thus a lower grain boundary density (fewer scattering centers), this translates to better transport properties.

A standard measure of merit for superconducting materials is the residual resistance ratio ( $RRR$ ), which is the ratio of a material's DC resistance at room temperature and just above  $T_C$ . For niobium,  $RRR$  is typically defined as

$$RRR = \frac{R_{300K}}{R_{10K}}. \quad (4.2)$$

Resistance in metals can be caused by things like impurity level [85], film thickness [86], and grain size [87], all of which lead to enhanced scattering. In  $RRR$  measurements, the resistance due to phonons is temperature dependent and is accounted for

by taking measurements at two temperatures. The other causes of resistance are temperature independent and therefore  $RRR$  can be used to gauge the effects of these scattering mechanisms. Because the Nb/MgO films were prepared under comparable conditions (base pressure, working pressure, target purity, growth rate, etc.),  $RRR$  values can be used as a relative gauge of grain boundary density.  $RRR$  values were measured for thicker films ranging from 500-1000 nm. Consistent with the discussion on the Nb(110) films having a higher grain boundary density, these films had overall lower  $RRR$  values, ranging from 26-46.5, while the Nb(100) films had higher  $RRR$  values ranging from 158-165.5. It should be noted that  $RRR$  values are highly dependent on film thickness and even larger values have been reported for Nb/MgO films much thicker than the samples reported here [88].

We note a strong relationship between the film epitaxy and the resulting surface morphology evidenced in AFM scans as shown in Figure 4.4. Figure 4.4 (a) shows surface features with a regular distribution and 4-fold symmetry that is consistent with the earlier discussion on Nb(100)/MgO(100) epitaxy. Likewise, for the case of Nb(110) surfaces such as the one shown in Figure 4.4 (b), there are features with strong uniaxial anisotropy that are oriented perpendicular with respect to each other. These surface features correlate well with the possible epitaxial orientations shown in Figure 4.1. The scaling of these features with increasing thickness has also been studied [89].

Because SRF performance is highly dependent on the quality of the surface morphology which in turn is correlated to the microstructure, it is necessary to under-

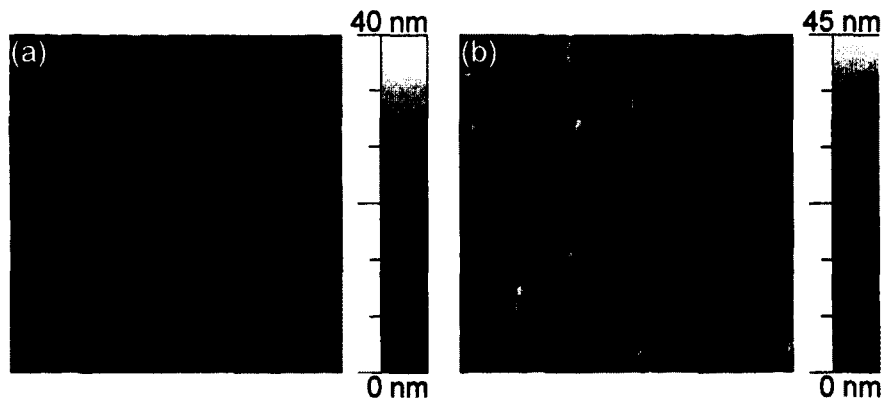


Figure 4.4: Representative AFM scans for (a) Nb(100) and (b) Nb(110) surfaces. The scan size for both images is  $2 \mu\text{m} \times 2 \mu\text{m}$ .

stand how the microstructure in the Nb/MgO(100) films affects their superconducting properties. The superconducting properties, in particular  $T_C$  and  $H_{C1}$ , were measured using the previously discussed methods (the procedure presented in reference [71] was used for measuring  $H_{C1}$ ) and are summarized in Table 4.1.

Thickness (nm)	Nb(100)		Nb(110)	
	$T_C$ (K)	$H_{C1}$ (Oe)	$T_C$ (K)	$H_{C1}$ (Oe)
100	9.2	1300	9.2	600
500-600	9.2	1600	9.3	1200
1000	9.3	1800	9.2	1700

Table 4.1: Summary of superconducting properties.  $T_C$  values were measured with an applied field of 50 Oe.  $H_{C1}$  values were measured at 4 K.

For all films measured,  $T_C$  values (measured with an applied magnetic field of 50 Oe) were close to the value for bulk niobium. However, for all films thicknesses, the Nb(100) films consistently had higher  $H_{C1}$  (measured at 4 K) values than their Nb(110) counterparts suggesting that the increased grain boundary density leads to



enhanced magnetic field pinning sites and hence worse superconducting properties.

While some of our measured  $H_{C1}$  values are larger than values that have been measured for bulk samples [90], a recent study by Roy *et al.* suggests that the penetration field may be larger than previously reported values [91]. This study finds that the penetration field value depends on the sample shape and surface condition and cites measured penetration field values of at least 2000 Oe at 3 K.

Having now examined how grain boundary density can affect microstructure, surface morphology, and superconducting films in an ideal situation, a similar study was carried out for Nb films deposited on copper surfaces in order to explain previous shortcomings on niobium coated copper cavities.

For the present studies, clean copper surfaces were obtained by depositing copper onto hydrofluoric acid etched Si(100) which results in a Cu(100) surface [92]. This procedure was chosen to avoid native oxides that are present on copper that has been exposed to atmosphere and the surface treatments required to remove this oxide that might have complicated the analysis of the subsequent niobium growth. Additionally, mild annealings have been shown to smoothen the copper surfaces after annealing [93] [94].

As was done in the previous case of MgO(100) substrates, we need to discuss the possible epitaxy in the case of niobium deposited onto Cu(100). In this case, niobium will grow oriented (110) out of plane with four possible in plane orientations such that the full epitaxial relationship can be described as

$$Nb(110)[111] \parallel Cu(100)[110] \quad (4.3)$$

leading to a greater grain boundary density than on MgO(100) substrates [83]. A visual depiction of the four possible orientations is shown in Figure 4.5.

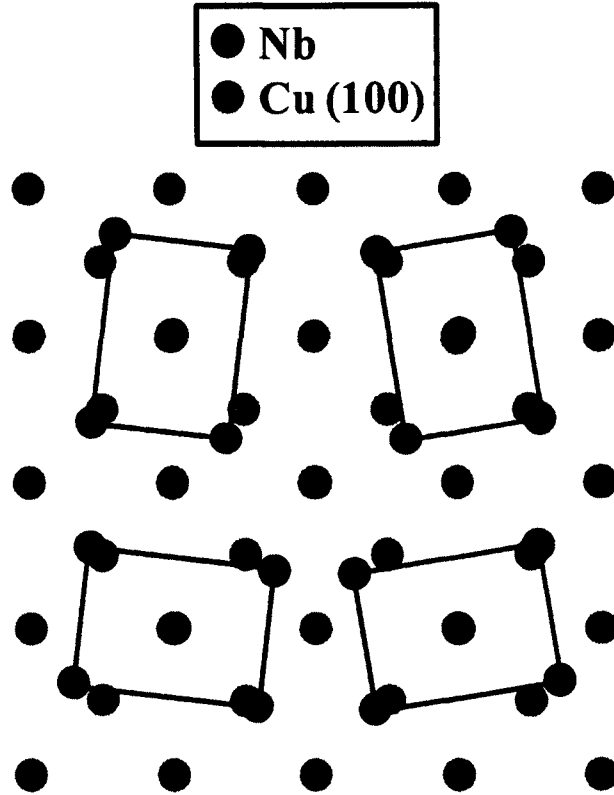


Figure 4.5: Overlays of relaxed niobium lattices on a Cu(100) surface.

For the Nb(110)/Cu(100) study, two types of samples were prepared. Both types began with 500 nm Cu deposited onto the HF-etched Si(100) substrates. Subsequently, 500 nm Nb films were deposited using similar conditions as those used for the Nb/MgO(100) study with the exception of growth temperature. One type of Nb(110)/Cu(100) had a niobium deposition temperature of 150 °C while the other

type had niobium deposited at room temperature. It was necessary to constrain the growth temperature to below 175 °C in order to prevent temperature driven reactions at the Cu-Si interface [95]. The RHEED characterization of these films again agrees with the expected epitaxy as shown in Figure 4.6 (a). In contrast to the previous study, the streaks in Figure 4.6 (a) are much broader streaks indicating a smaller average lateral grain size. The superposition of two streak spacings in Figure 4.6 (a) along the Si[100] direction that have a  $\sqrt{2}$  ratio indicate the formation of orthogonal Nb(110) domains. The patterns along the Si[110] directions correspond to the contributions mentioned earlier along the MgO[110] direction for Nb(110) [83].

The surface morphology of the Nb(110)/Cu(100) films (Figure 4.6 (b)) have features similar to those seen in Nb(110)/MgO(100) samples. For the Nb(110)/Cu(100) samples, these surface features were finer for the room temperature growths than for the samples prepared at 150 °C. Correspondingly, the room temperature samples had a lower RMS roughness (1.98 nm) than the 150 °C samples (2.87 nm).

XRD measurements showed that the films exhibited less than 1% strain, similar to the case of Nb/MgO growth. The samples grown at room temperature had an average grain size of  $44 \pm 2$  nm while the growth at 150 °C lead to an average grain size of  $50 \pm 2$  nm indicating that the increased growth temperature allowed for the formation of larger grains.

When the superconducting properties of both types of Nb(110)/Cu(100) were measured, both types had typical  $T_C$  values around 9.2 K but the sharpness of the transitions was quite different as shown in Figure 4.7. The films grown at 150 °C had

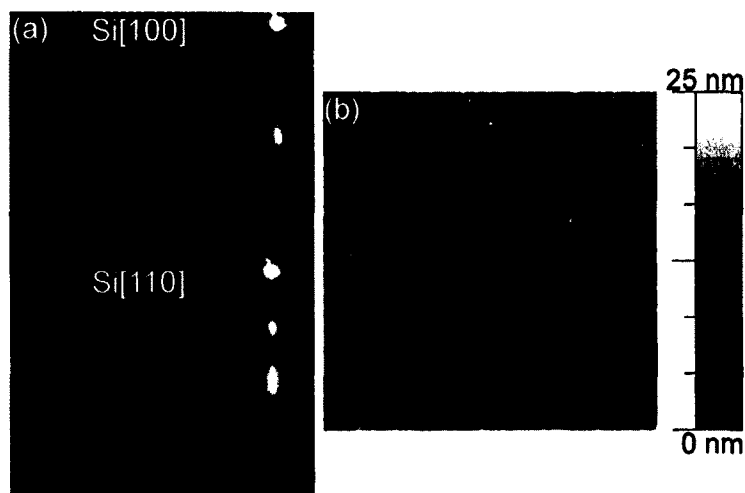


Figure 4.6: (a) RHEED pattern for Nb(110)/Cu(100)/Si(100) along the Si[100] and Si[110] azimuths. (b) A representative  $2 \mu\text{m} \times 2 \mu\text{m}$  AFM scan for niobium films on the Cu(100)/Si(100) template.

a very sharp transition that begins at  $\sim 9$  K, while the room temperature films begin to transition into the normal state at  $\sim 7$  K.

When the  $H_{C1}$  values were measured using the procedure in reference [71], the room temperature growth was found to have  $H_{C1} = 50$  Oe while the  $150^\circ\text{C}$  growth had  $H_{C1} = 100$  Oe. These values are on the same order of magnitude as other reports of sputtered niobium films [30].

Our results suggest that an increased deposition temperature of niobium onto copper surfaces leads to films with higher crystalline quality (i.e. grain size) and thus improved superconducting properties (i.e.  $H_{C1}$ ). This increased deposition temperature also lead to an improvement in the sharpness of the superconducting to normal state transition. Therefore, it is likely that when niobium coated copper cavities are fabricated, their performance would benefit from deposition at a temperature greater

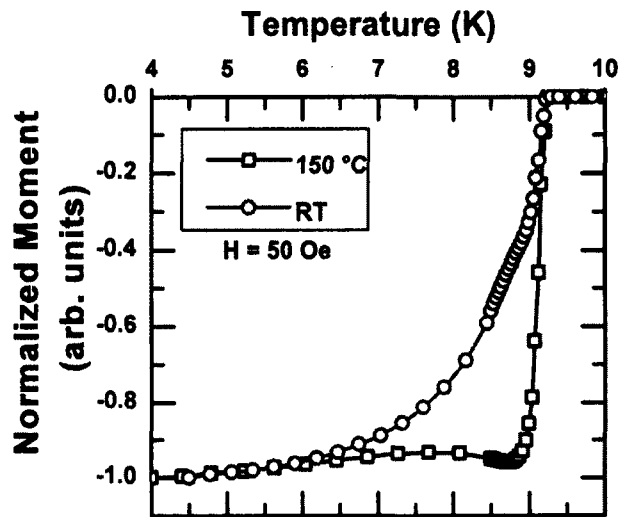


Figure 4.7: Critical temperature transitions for films deposited at room temperature and 150 °C.

than 150 °C during niobium deposition.

Since increased grain boundary density can have detrimental effects on the superconducting properties of thin films, efforts should be focused on decreasing it in order to improve the performance of niobium coated copper cavities. One possible method to accomplish this is the use of a seed layer (or layers) between the copper and niobium that decreases the number of possible epitaxial orientations for niobium. This should be the focus of future work. Also, since large grain copper substrates may have other out of plane orientations, a systematic study of depositing niobium onto Cu(110) and Cu(111) surfaces should also be carried out.

## 4.2 The Effect of Interfacial Strain

As discussed in the previous section, there are many material factors that can have detrimental effects on the performance of superconducting thin films. In this section, we examine the effect of interfacial strain in the case of niobium films deposited onto a-plane sapphire. The growth of niobium onto sapphire substrates has been studied extensively [96]. For the specific case of niobium on a-plane sapphire, the epitaxial relationship is

$$Nb(110)[\bar{1}00] \parallel Al_2O_3(11\bar{2}0)[0001] \quad (4.4)$$

which leads to a 10.7% lattice mismatch along the Nb[100] direction and 8.3% along the Nb[110] direction.

The a-plane sapphire substrates were annealed at 600 °C for one hour prior to the niobium deposition which was carried out at a working pressure of 5 mTorr Ar. Niobium film growth was studied up to a thickness of 600 nm. The microstructure of the films was investigated using *in situ* RHEED and *ex situ* using XRD and transmission electron microscopy (TEM).

In order to determine the evolution of the in plane strain, a measurement of the lattice parameter was carried out for thicknesses ranging from 1 to 63 atomic layers. Because RHEED cannot operate in the pressure range of the niobium growth (due to lack of differential pumping), each measurement was taken after interrupting the growth process and pumping the Ar from the system. Initially, two RHEED patterns

appeared that repeated every  $60^\circ$  indicating a hexagonal niobium structure (the two patterns were separated by  $30^\circ$  from each other). Following the first three atomic layers, the niobium film transformed into a mixed hexagonal and bcc phase for two atomic layers before fully reverting to its native bcc structure. After changing to the bcc structure, the niobium film kept growing strained until about 14 atomic layers where it approached the bulk niobium lattice parameter. The measured lattice parameters corresponding to the evolution from a hexagonal to mixed to bcc phase is shown in Figure 4.8. This initial hexagonal phase was previously reported by Oderno *et al.* but they did not report on further evolution of the lattice parameter after transitioning from the initial hexagonal phase to the native bcc phase [97].

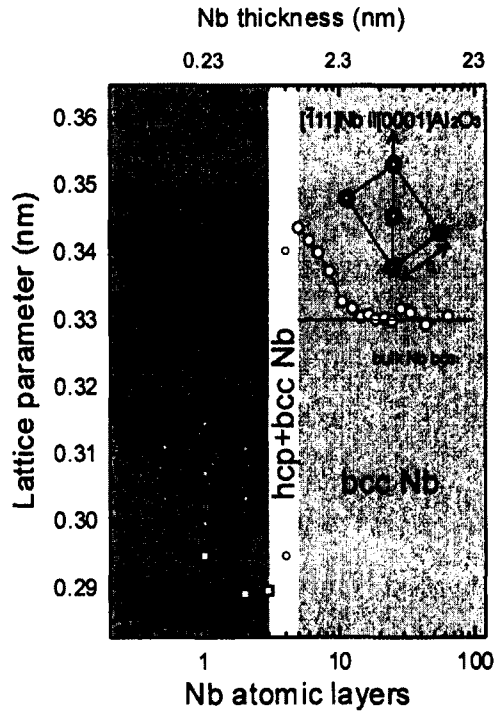


Figure 4.8: Evolution of niobium structure and lattice parameter as the film's thickness increases from 1 to 63 atomic layers. Full relaxation into the bcc phase occurs after 14 atomic layers.

The RHEED analysis probing the in plane lattice parameter indicates that niobium films deposited onto a-plane sapphire follow two mechanisms to overcome the lattice mismatch between the two materials. First, niobium forms a two-dimensional hexagonal phase, deviating from its native bcc structure and, after transitioning to a strained bcc structure, it progressively relaxes to bulk like lattice parameter.

The out of plane lattice parameter was also probed using XRD. It should be noted that XRD probes the entire thickness of the film and therefore only provides an average lattice parameter. The out of plane lattice parameter for 30 nm, 100 nm, and 600 nm niobium films were found to be 1.25%, 0.36%, and 0.2% respectively



larger than bulk niobium. It is expected that the interfacial strain would have a significantly smaller contribution for thicker films and therefore it is not surprising that the average strain decreases as film thickness increases.

In order to better determine the out of plane lattice parameter near the interface, cross sectional TEM was used to investigate the interface as shown in Figure 4.9. The TEM images revealed a very sharp interface with high quality crystalline structure in both the sapphire and the niobium. Two dimensional FFTs were used to analyze the out of plane atomic spacing. For the sapphire substrate, the lattice parameter matched the expected 2.37 Å. For the entire thickness of the niobium film examined in Figure 4.9, the niobium also exhibited a spacing of 2.37 Å, 1.72% larger than the bulk Nb(110) spacing of 2.33Å indicating that the niobium film was matching the substrate spacing through a continuous transfer of lattice planes [98].

Once the microstructure had been characterized and it was determined that there existed two phases in niobium films on a-plane sapphire (one strained phase near the interface and one relaxed phase away from the interface), the superconducting properties of the films were measured to determine the effect of the two phases. The transition from the superconducting state into the normal state was measured using SQUID magnetometry with an AC field of 3.5 Oe at 1.5 Hz superimposed onto a 100 Oe DC field parallel to the film surface. When SQUID is operated in AC mode, the frequency-dependent complex susceptibility can be expressed as

$$\chi(\omega) = \chi'(\omega) + i\chi''(\omega) \quad (4.5)$$

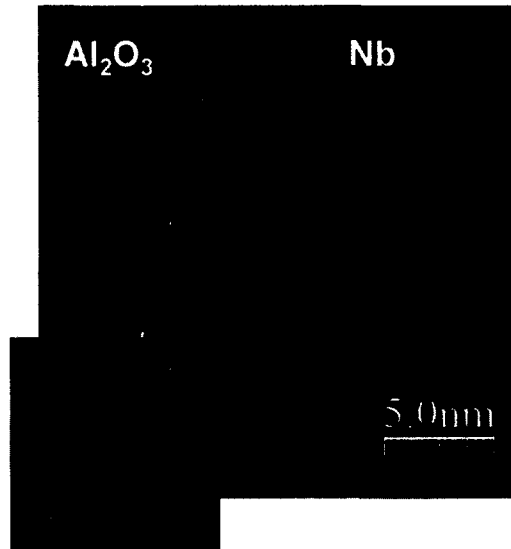


Figure 4.9: TEM image at the interface of sapphire and niobium. Inset shows a representative region (and FFT of the region) used to measure the spacing between atomic planes.

where the real part,  $\chi'(\omega)$ , describes the sample's response to the applied field and the imaginary part,  $\chi''(\omega)$ , describes the energy losses in the sample. Figure 4.10 shows the AC susceptibility for a 30 nm, 100 nm, and 300 nm niobium film on a-plane sapphire.

The  $T_C$  values were found to be 8.75 K and 8.7 K for the 100 nm and 600 nm films respectively. It should be noted that the presence of a 100 Oe field during measurement lead to a decreased  $T_C$ . Resistive measurements (no field applied) of the 600 nm film found a  $T_C$  of 9.29 K and a RRR of 97, one of the largest values obtained for niobium films on sapphire [99] [100]. While the 100 nm and 600 nm films exhibited only a single step in the  $\chi'$  vs. T curve, the 30 nm film's curve had two steps. Correspondingly, there are two peaks in the  $\chi''$  vs. T curve at 7.64 K and 8.08

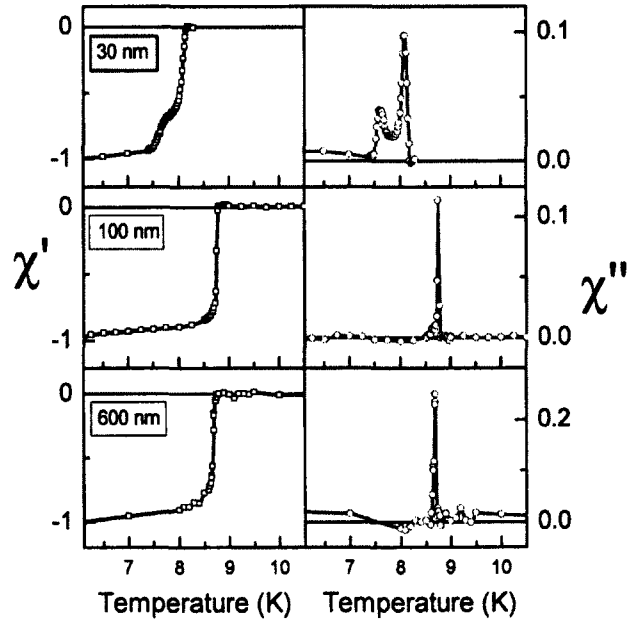


Figure 4.10: (left) Real  $\chi'$  and (right) imaginary  $\chi''$  parts of the susceptibility for 30 nm, 100 nm, and 600 nm niobium films on *a*-plane sapphire.

K. The presence of multiple peaks in the  $\chi''$  component of the susceptibility has been attributed to transport through grain boundaries [101] [102].

Correlating the superconducting response of these films, the observed response of the 30 nm film can be attributed to the presence of two phases in the sample: one with poor superconducting properties due to strain and proximity to the interface and a second with relaxed niobium that exhibits behavior more akin to bulk niobium. While both of these phases are present in the thicker films, they contain more relaxed niobium and therefore the contribution of the strained phase at the interface is significantly diminished.

When implementing SIS multilayers in SRF cavities, it will be necessary to account for the effect of interfacial strain. Because the thicknesses involved in the multilayers

are on the order of tens of nanometers, each layer will be affected by any strain found near interfaces. Since these strained regions lead to poorer superconducting properties compared to the relaxed regions, the overall performance can be diminished compared to theoretical predictions due to the presence of multiple interfaces. This work has provided new insights relating microstructure and superconducting properties for the identification of dissipative effects associated with strained regions and defects related to the early stages of film growth.

### 4.3 Niobium Nitride Thin Films

Before Gurevich's SIS model can be implemented successfully, it is necessary to understand how the thin film geometry, microstructure, and surface morphology will affect the superconducting performance of the films that are used to shield the underlying niobium cavity. For the work presented here, efforts are focused on niobium nitride (NbN). NbN can be prepared using a variety of deposition techniques, for example DC reactive sputtering [103] [104], RF reactive sputtering [105] [106], pulsed laser deposition [107], and laser nitriding [108]. Preliminary studies on NbN based multilayers have demonstrated the plausibility of the SIS model [29].

The NbN films in this study were prepared using DC magnetron reactive sputtering using a 99.95% pure niobium target. The total working pressure was fixed at 3.4 mTorr and the partial pressure of N<sub>2</sub> gas was varied from 5.9-26.5% in order to optimize the stoichiometry and structure to achieve the desired properties. MgO(100)

substrates that had been annealed for one hour at 600 °C and subsequently had 3 nm fresh MgO deposited on the surface using pulsed DC reactive sputtering (using a Mg target and an Ar/O<sub>2</sub> gas mixture) were used. The fresh MgO layer improves the quality of the substrate surface by minimizing step edges along terraces due to miscut. NbN films with a thickness of 200 nm were deposited at a substrate temperature of 600 °C to assess microstructure-superconducting properties correlations.

One major difference between the proposed SIS model and current technology is that the interior surface of the SRF cavity will be coated with a different material. Since SRF performance is highly dependent on the cavity surface quality [5], a variety of surface processing methods such as electropolishing [109], buffered chemical polishing [110], and plasma treatments [111] have been explored to achieve the highest quality possible with bulk niobium surfaces. Achieving bulk like properties in thin films is a non-trivial problem since the normal dimension is severely constrained and the material type, growth technique, and substrate conditions can affect the final surface morphology and overall properties of thin films [112] [113] [114] [115].

Metallic films, such as niobium, tend to grow in three-dimensional island (Volmer-Weber) or layer plus island (Stranski-Krastanov) growth modes which are often affected by the presence of step-edge diffusion barriers during growth [116] leading to rough surfaces that may not be optimal for SRF applications. Lattice mismatch between the film and substrate can also affect the early stages of growth promoting three dimensional growth mode [117]. Thick niobium films can also develop faceted surfaces [96].

On the other hand, when reactive sputtering is used to deposit compounds, high reactive gas concentrations can completely cover the film's islands of all orientations. This coverage helps prevent significant coarsening during coalescence of islands and film growth proceeds by repeated re-nucleation. The advantage of repeated re-nucleation is that surface faceting and related shadowing effects are eliminated leading to films that are inherently smoother and also more dense [118].

An initial step to understanding potential differences between SIS multilayered structures and current technology is to investigate how the surface evolves after depositing the SIS subsequent layers (in this case NbN) compared to pure Nb. AFM scans obtained for NbN surfaces were compared to the Nb(100) and Nb(110) surfaces deposited on MgO(100) that were previously discussed. The NbN surfaces exhibited small isotropic features as shown in Figure 4.11 (a). Surface topography for Nb(100) and Nb(110) films of comparable thickness and growth conditions are shown Figure 4.11 (b) and (c) respectively. Representative line scans for these surfaces are displayed in 4.11 (d). All of the NbN films had RMS roughness values  $< 1$  nm, lower than the 1.21 nm for Nb(100) and 2.45 nm for Nb(110).

In addition to comparing RMS roughness values, additional information about the surface morphology can be obtained after PSD analysis. Figure 4.12 shows the PSD versus  $k$  curves corresponding to the surfaces shown in Figure 4.11. For the curves corresponding to the Nb(100) and Nb(110) surfaces, there is a peak present at  $-1.5$   $\text{nm}^{-1}$  and  $-1.9$   $\text{nm}^{-1}$ , while no such peak is present for the NbN curve. The peaks present in the niobium PSD curves are indicative of wavelength selection associated

with Schwoebel barriers affecting the surface morphology during growth [119]. The absence of such peaks in the NbN PSD curve indicates that no step edge diffusion barrier affected the growth and that isotropic surface features formed in a self-affine manner [120].

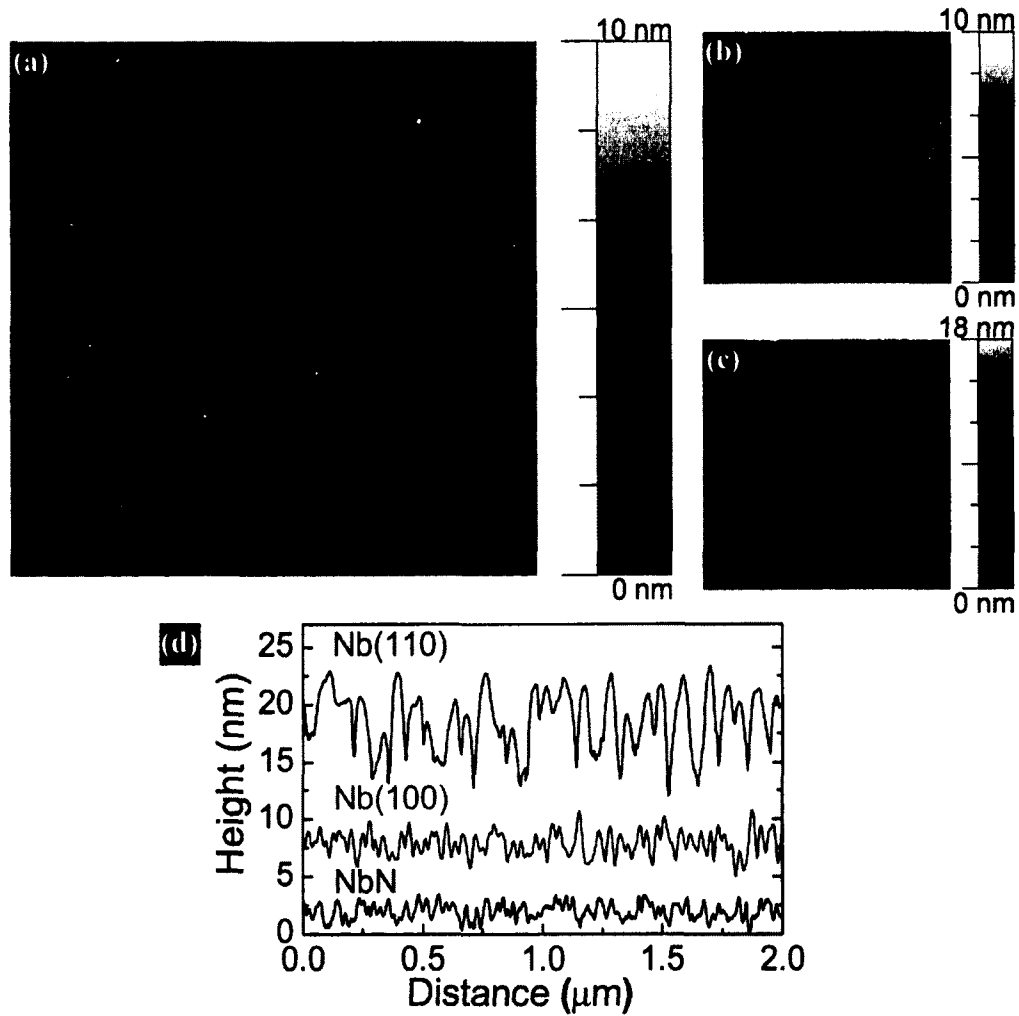


Figure 4.11: AFM images of (a) NbN, (b) Nb(100), and (c) Nb(110) surfaces. All scan sizes are  $2 \mu\text{m} \times 2 \mu\text{m}$ . RMS surface roughness is  $<1 \text{ nm}$  for NbN,  $1.21 \text{ nm}$  for Nb(100), and  $2.45 \text{ nm}$  for Nb(110). (d) Representative line scans for the three surfaces.

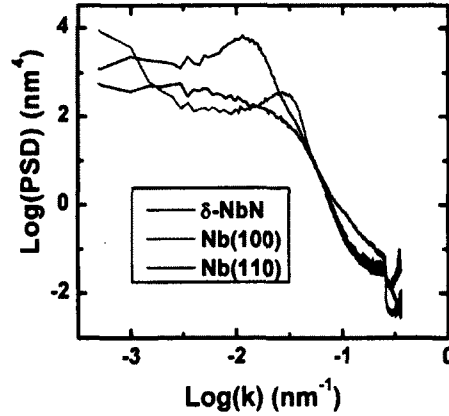


Figure 4.12: PSD versus  $k$  for NbN, Nb(100), and Nb(110). The absence of a peak in the NbN curve indicates that the surface is exhibiting self-affine growth.

Because the NbN phases present in thin films can be tailored by altering the partial pressures of Ar and N<sub>2</sub> while holding the total pressure constant [121], it is necessary to achieve the desired NbN phase since only the  $\gamma$  and  $\delta$  phases are superconducting. The  $\gamma$  phase forms a body centered tetragonal structure (space group  $I4/mmm$ ) while the  $\delta$  phase forms a rocksalt cubic structure (space group  $Fm\bar{3}m$ ) [122]. In addition to the structural difference between the two phases, the  $\gamma$  phase has  $T_C$  values that range from 12-15 K while the  $\delta$  phase has  $T_C$  values that range from 15-17.3 K [123]. Even if only one of the superconducting phases is present in a film, the transition temperature can still be highly dependent on the partial pressures used during growth [124]. Figure 4.13 shows XRD scans for the films presented here that contain only  $\delta$ -NbN.

The lattice parameters along the  $a$  and  $c$  directions (obtained from symmetric and asymmetric scans respectively) are presented in Figure 4.14 (a). The  $c/a$  ratios for all partial pressures are within 1% of 1 correlating to the presence of the  $\delta$  phase. Out of



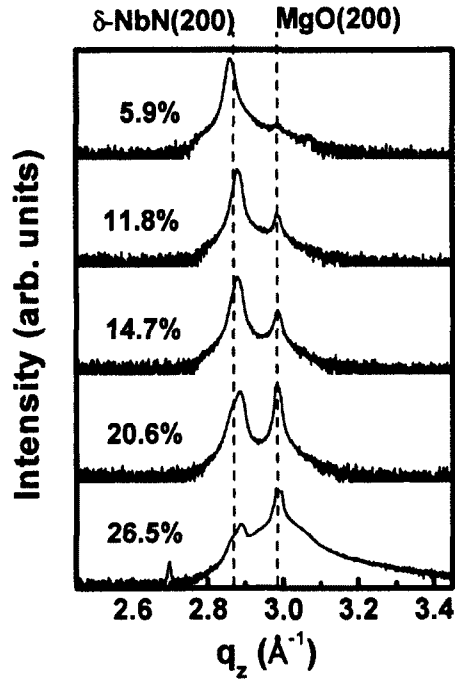


Figure 4.13: XRD scans for varying nitrogen partial pressure. The vertical dashed lines represent the positions for  $\delta$ -NbN (lower end of range presented in text) and MgO.

all of the  $N_2$  partial pressures used, only the 5.9% produced a lattice parameter that lies within the range of reported bulk  $\delta$ -NbN values (4.378-4.42Å) [125]. The average grain size generally increases as the nitrogen partial pressure decreases as shown in Figure 4.14 (b). Because all scans in Figure 4.13 were carried out optimized for the NbN(200) peak and the MgO(200) peak intensity increases with increasing nitrogen partial pressure, this indicates that a higher nitrogen partial pressure leads a better alignment of atomic planes in the film with respect to atomic plans in the substrate. The quantified degree of misalignment between the film and substrate planes is shown in Figure 4.14 (c). The films that were deposited at lower nitrogen partial pressures had a lower degree of mosaicity as shown in Figure 4.14 (d).

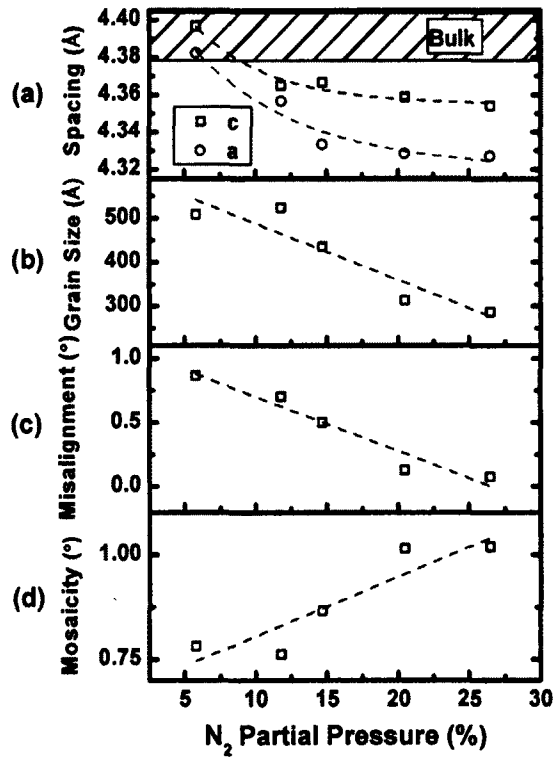


Figure 4.14: (a) Lattice parameter for the *c* and *a* directions, (b) average grain size, (c) misalignment between NbN(200) and MgO(200) planes, and (d) degree of mosaicity of the NbN(200) reflection versus nitrogen partial pressure. All dashed lines are guides to the eye.

Asymmetric XRD scans were carried out for the NbN(220) and MgO(220) peaks in order to determine the in plane orientation of the film with respect to the substrate. A representative scan is shown in Figure 4.15. The four peaks separated by 90° confirm the presence of a cubic film and substrate. Because the NbN and MgO peaks align at the same  $\phi$  values, the NbN film is not rotated in plane with respect to the substrate and therefore grew cube on cube.

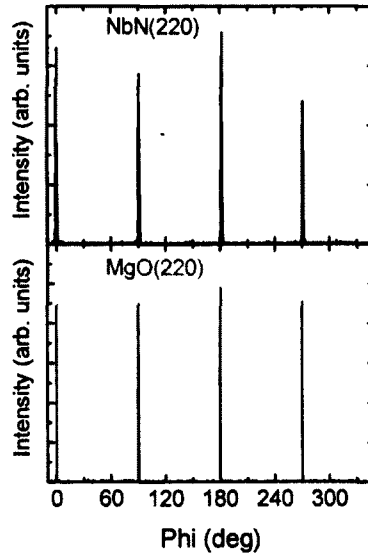


Figure 4.15: Asymmetric scans for the NbN(220) and MgO(220) peaks indicating cube on cube growth.

$RRR$  measurements were carried out in the same manner as previously discussed with the exception that

$$RRR = \frac{R_{300K}}{R_{20K}}. \quad (4.6)$$

was used since NbN has a higher  $T_C$ . A typical resistivity plot for the  $\delta$ -NbN films is shown in Figure 4.16. The films with a bulk like lattice parameter had  $RRR$  values of 1, which is consistent with previous reports indicating a lack of detectable voids and defects between grains [126] [127]. It should be noted that  $RRR$  values of compound films such as NbN drastically differ from those of metallic films like niobium who typically have  $RRR$  values much larger than 1. As shown by Jones [127], there is a strong correlation between  $T_C$  and  $RRR$  values in NbN films where the resistance of

the films increases with decreasing temperature when a film's  $T_C$  is much lower than that of the bulk material. On the other hand, when a film's  $T_C$  approaches the bulk value, the rise of resistance at low temperatures is significantly depressed. Since the measured  $RRR$  values for our films is 1 (resistivity is independent of temperature), this suggests that the electron transport is not dominated by a granular structure in the films.

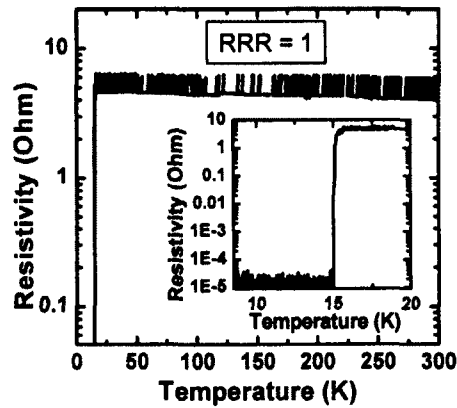


Figure 4.16: Resistivity as a function of temperature in a  $\delta$ -NbN phase film. Inset shows the superconducting transition.

When the  $T_C$  values were measured, shown in Figure 4.17, a trend was found that was similar to the trend found for the lattice parameters as a function of nitrogen partial pressure. As the nitrogen partial pressure decreased,  $T_C$  values increased and bulk like values were only achieved for a 5.9% partial pressure.

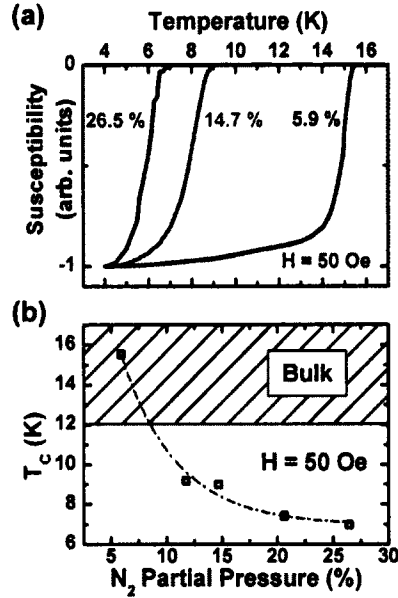


Figure 4.17: (a) Superconducting response as a function of temperature for 5.9%, 14.7%, and 26.5% nitrogen partial pressure films. (b)  $T_C$  as a function of nitrogen partial pressure. These measurements were carried out with a 50 Oe applied field parallel to the film surface. Bulk values range from 12-15 K for the  $\gamma$  phase and 15-17.3 K for the  $\delta$  phase of NbN. Dashed line is a guide to the eye.

When the  $H_{C1}$  values were measured using the procedure described in reference [71], it was found that the films grown at a 5.9% nitrogen partial pressure, the films that exhibited both a bulk like lattice parameter and  $T_C$ , had an  $H_{C1}$  value of 1100 Oe which is consistent with previously reported values [128]. All other films had  $H_{C1}$  value of 400-500 Oe. Representative measurements are displayed in Figure 4.18.

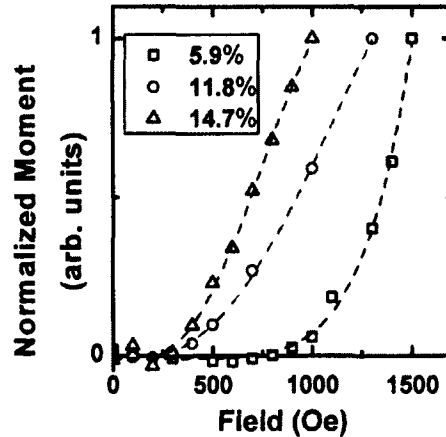


Figure 4.18: The difference between a sample's magnetic moment before and after a magnetic field is applied as a function of that applied field. The jump in this difference around 400 Oe for 14.7%, 500 Oe for 11.8% and 1100 Oe for 5.9% indicate the remnant fields and therefore penetration at that applied field. The dashed lines are guides to the eye.

If NbN films are to be considered as models in order to improve SRF performance of accelerators, they must have optimal superconducting properties. As shown above, preparing NbN films using a reactive sputtering process allows the superconducting and structural properties to be tailored while also producing films that are inherently smoother and denser than those obtained with alternative deposition methods. For successful deposition onto the interior surface of cavities, the growth process will need to be further optimized. As shown here, the argon-nitrogen ratio can affect structural properties such as lattice parameter, grain size, alignment of the film with respect to the substrate, and mosaicity as well as superconducting properties such as transition temperature and lower critical field.

In the next section, NbN films are incorporated in a multilayer structure to test their ability to shield an underlying niobium film. These proof of principle samples

will provide insight into whether Gurevich's SIS model is feasible.

## 4.4 NbN/MgO/Nb Trilayers

Thin film multilayer structures were prepared on MgO(100) substrates to produce proof of principle SIS structures to test the shielding ability of Gurevich's model. First, a niobium film was deposited to represent the cavity that is to be shielded. Subsequently, an insulating layer of MgO and superconducting layer of NbN were deposited using reactive sputtering to form the structure shown in Figure 4.19. The microstructure of the films was investigated using XRD and the superconducting properties were determined using SQUID magnetometry.



Figure 4.19: Cross sectional representation of proof of principle trilayer samples.

For the multilayer study, two types of structures were fabricated:

Type 1: 30 nm NbN / 15 nm MgO / 600 nm Nb / MgO(100) (4.7)

Type 2: 50 nm NbN / 15 nm MgO / 250 nm Nb / MgO(100)

Because the NbN films in these structures are much thinner than the range of London



penetration depths reported ranging from 100 nm [129] to 400 nm [130], an enhancement of  $H_{C1}$  should occur following Equation (2.16). Therefore, vortex penetration should occur at fields higher than those reported in the previous section. By changing the thickness of the underlying niobium film, the template surface on which the rest of the multilayer is deposited on is also changed. In these multilayers, the quality of the NbN will be affected since they are now deposited on rougher surfaces as opposed to an ideal atomically flat surface. In general, as the film thickness increases, the surface roughness will also increase. To demonstrate this, representative topography line scans for Nb(100)/MgO(100) films with thicknesses ranging from 10-1000 nm are shown in Figure 4.20.

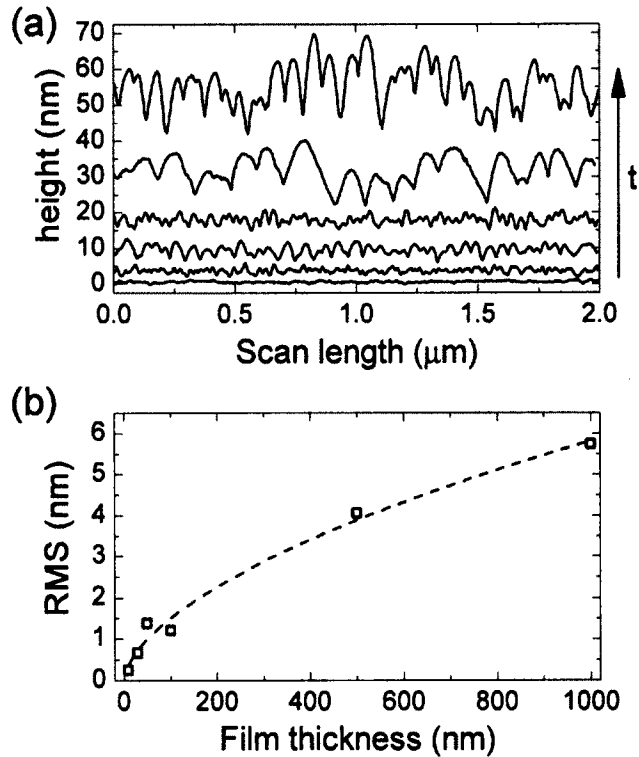


Figure 4.20: (a) Representative topography line scans for 10 nm, 30 nm, 50 nm, 100 nm, 500 nm, and 1000 nm thick Nb(100)/MgO(100) films. As film thickness,  $t$ , increases the surface roughness increases. (b) RMS roughness as a function of film thickness. The dashed line is a guide for the eye.

The orientation of the films in the multilayer structures was determined using XRD as shown in Figure 4.21. For both types of multilayers, the initial niobium film grew in the (200) orientation. As discussed earlier, this orientation of niobium tends to be of higher quality than the (110) orientation due to a lower grain boundary density. The NbN layers at the surface for both types formed the superconducting  $\delta$  phase in the (200) orientation as well.

When the superconducting properties of the multilayers were measured, the  $T_C$  of the NbN films were lower than previously studied NbN films as shown in Figure 4.22.

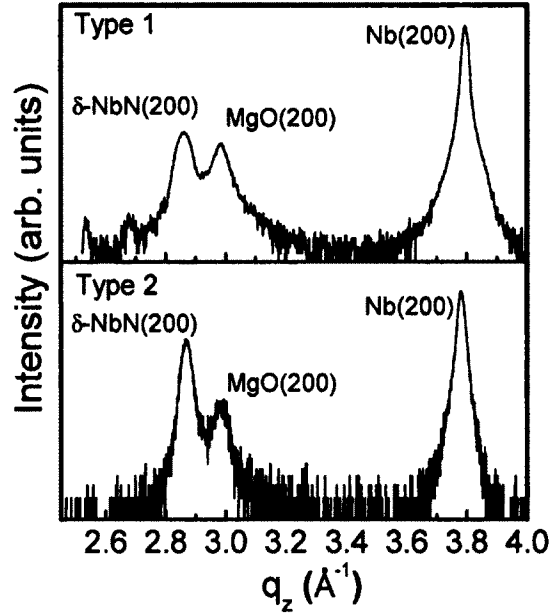


Figure 4.21: Representative XRD scans of Type 1 and Type 2 samples. The only orientation of niobium seen is the (200) orientation. The surface layer of NbN forms the superconducting  $\delta$  phase also oriented in the (200) orientation.

A typical Type 1 multilayer had a NbN  $T_C$  of 10.5 K and typical Type 2 multilayer had a NbN  $T_C$  of 12.2 K despite using growth conditions that had produced films with a  $T_C$  up to 15.5 K.

This decrease in  $T_C$  can be attributed to a lower crystal quality due to the rougher surface on which the NbN films were deposited, demonstrating how in the case of thin films, as in the case of bulk surfaces, the quality of the surface is of paramount importance.

In order to determine the value of the applied field at which vortices penetrate into the multilayer, isothermal  $m(H)$  loops were measured using SQUID magnetometry. A representative loop is shown in Figure 4.23 (a). The penetration field,  $H_P$ , is determined as the point at which the  $m(H)$  curve deviates from the initial linear

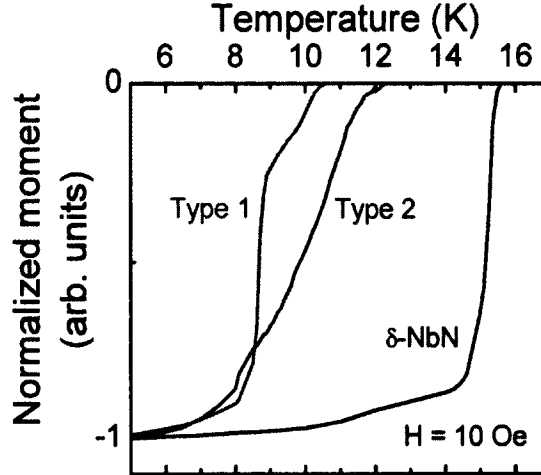


Figure 4.22:  $T_C$  measurements for a Type 1, Type 2, and  $\delta$ -NbN/MgO(100) samples. The step that appears at  $\sim 8$  K for the Type 1 and Type 2 samples represents the niobium film transitioning into the normal state.

region where the sample is fully in the Meissner state. Figure 4.23 (b) and (c) show the initial linear region and subsequent deviation for typical Type 1 and 2 samples. For both types,  $H_P$  occurs around 2000 Oe, larger than  $H_{C1}^{Nb}(0K) = 1700$  Oe. This is the first time that the penetrating field measured surpassed that of bulk Nb and it is therefore a significant improvement over  $H_P=960$  Oe that was achieved by Antoine *et al.* [29] [30].

As discussed by Antoine [30], even though the niobium in this test structure is only shielded on one side by the NbN, the shielding provided is sufficient to affect the *effective* field that is experienced by the niobium layer. Based on the results presented in Table 4.1, the expected  $H_{C1}$  values for niobium films of the thickness in these proof of principle samples are around 1300-1600 Oe. In fact, the critical field values for niobium ( $H_{C1}=1700$  Oe and  $H_C=2000$  Oe) are quoted for 0K while the SQUID

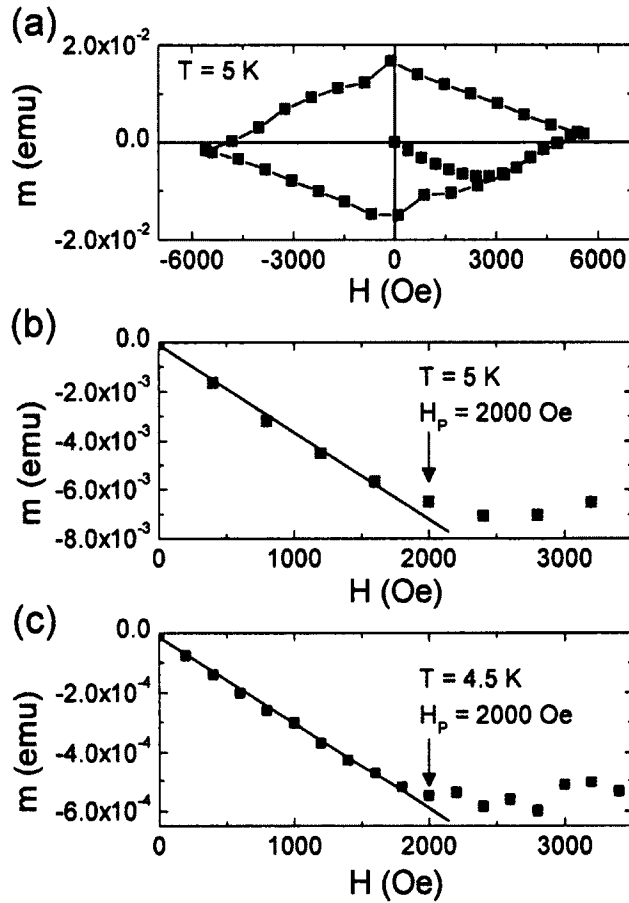


Figure 4.23: (a) Full  $m(H)$  behavior for a Type 1 sample at  $T = 5$  K. (b) Initial linear region for a Type 1 sample. The Meissner state is preserved to at least  $H = 1600$  Oe and there is not obvious field penetration until  $H = 2000$  Oe. (c)  $m(H)$  behavior for a Type 2 sample at  $T = 4.5$  K where  $H_p$  occurs at  $2000$  Oe.

measurements were carried out at 4-5K. In this temperature range, even an extremely pure and pristine niobium sample is not expected to achieve  $H_p = 2000$  Oe. Therefore, we conclude that it is the presence of the NbN that delays vortex penetration to a higher applied field. Additionally, the shielding up to  $2000$  Oe is essentially an underestimate due to the alignment issues related to SQUID measurements that was discussed earlier.

For the first time, the ability to delay vortex penetration beyond the lower critical field of bulk niobium following Gurevich's SIS model has been demonstrated at 4-5K. This is an important accomplishment in order to implement suitable multilayer structures in SRF cavities with the hope of overcoming the accelerating gradient limit imposed by the use of bulk niobium. We should point out that RF surface impedance characterizations (SIC) constitute the ultimate test of the RF performance of these structures, but at present most SIC characterizations are carried out as a function of temperature thus only addressing RF losses. Since there isn't an RF SIC characterization as a function of applied field in place yet, the present penetrating field characterizations offers insight on the potential of magnetic field shielding. SIC measurements as a function of temperature in these samples are in progress.

# Chapter 5

## Summary and Outlook

### 5.1 Summary

Investigations of structure-property correlations in superconducting thin films and multilayers have been presented and discussed in this dissertation. In particular, the effect of film epitaxy and the resulting microstructure were correlated with superconducting properties such as transition temperature on lower critical field. Additionally, magnetic shielding beyond the lower critical field of niobium was achieved for the first time.

The study of niobium thin films on magnesium oxide and copper surfaces demonstrated how the number of possible epitaxial orientations can affect the ultimate superconducting properties of the thin film. Nb(100)/MgO(100) films with one in plane orientation consistently had larger  $H_{C1}$  values than their Nb(110)/MgO(100) counterparts that had two possible in plane orientations. Nb(110)/Cu(100) films

had  $H_{C1}$  values lower than either orientation on MgO(100), consistent with the fact that Nb(110) has four possible in plane orientations. Furthermore, it was found that an increased growth temperature of 150 °C lead to larger average grain sizes in Nb(110)/Cu(100) films when compared to films grown at room temperature. These larger grains lead to larger  $H_{C1}$  values in the films grown at 150 °C. Higher growth temperature also lead to sharper superconducting transition.

The strain found at the interface of a-plane sapphire and niobium films lead to the formation of two regions with different structures in niobium films. One region was a hexagonal phase combined with a strained bcc phase near the interface and the second was a relaxed bcc phase located away from the interface. When the superconducting properties of the films were measured, it was found that these two regions correlated to a double step in the superconducting transition. The strained region transitioned into the normal state at a lower temperature than the relaxed region. The AC susceptibility confirmed that systematic losses occurred at two different temperatures, corresponding to each structural region.

Niobium nitride films were fabricated that had properties desirable for SRF applications such as a higher  $T_C$  than niobium, a smooth surface, and transport properties indicating high quality films. When these films were implemented in proof of principle samples, magnetic shielding beyond the lower critical field off niobium was achieved for the first time, providing evidence that the SIS model may be successful if implemented in SRF cavities.

The results found throughout the work presented in this dissertation have sev-



eral implications for the SRF community as a whole. First, if thin films are to be successfully implemented, the epitaxial relationship with the substrate is crucial to achieving the desired superconducting properties. It was shown that epitaxial relationships with more possible in plane orientations led to films that generally had worse superconducting properties. If niobium coated copper cavities are to be implemented in the future, special care should be taken to provide a surface that allows niobium growth that minimizes grain boundary density. This may be achieved by using an appropriate seed layer (or layers) between the copper and niobium such that a better epitaxial relationship can be achieved. For example, if a seed layer is found that results in only one possible in plane orientation (much like the case of Nb(100)/MgO(100)), the number of possible relations would decrease from four to one. Of course, since bulk copper cavities will contain multiple orientations of copper, this seed layer must reduce the possible in plane orientation for each of the surfaces.

The second, and perhaps more important, implication of the work here is the evidence supporting Gurevich's SIS model. It was demonstrated that an SIS structure was able to reduce the *effective* field experienced by a niobium film. Not only was the *effective* field reduced, but vortex penetration did not occur until an applied field larger than that for  $H_{C1}$  for bulk niobium. Since both the DC and AC measurements presented by Antoine *et al.* were comparable, it is reasonable to consider that this shielding will occur beyond bulk niobium's  $H_{C1}$  in an AC environment as well. If this technology is successfully scaled up and implemented, it will have great consequences for SRF accelerator facilities and defense applications. Accelerator facilities could

replace the current bulk niobium cavities with SIS coated cavities and therefore be able to achieve higher energy particle beams with the same size facility and also will be able to operate at somewhat higher temperature thus also lowering operation costs. Alternatively, smaller accelerators with some degree of portability could be fabricated for defense applications such as the long range detection of fissile materials. But before SIS coatings can successfully be implemented, more research is needed. In the following section, a suggested road map to achieving successful implementation is presented.

## 5.2 Outlook

The majority of the research focusing on Gurevich's SIS model up until this time has dealt with small flat samples for which academic research grade instruments are designed for. The next step is to scale up the deposition processes to handle "larger" flat samples. NbN based multilayers, similar to the ones presented in this dissertation, have been fabricated on two inch diameter copper substrates. First, a niobium film was deposited using an electron cyclotron resonance source. The subsequent MgO and NbN layers were deposited using reactive sputtering. After growth, the surface resistance was measured as a function of temperature using the surface impedance characterization system described in [39]. The surface resistance of a representative multilayer is compared to niobium films prepared under similar conditions as well as large grain niobium in Figure 5.1. These results are encouraging

because the additional MgO and NbN layers do not seem to be detrimental to the residual resistance compared to just the niobium films. While the multilayers and niobium films are around the same order of magnitude in terms of surface resistance, there is still room for improvement to reach the level of large grain bulk niobium. Since the surface impedance cannot yet be measured as a function of applied field, it is not possible to evaluate the RF penetration field for these small samples. Other groups have also scaled up their deposition processes to produce two inch samples of  $\text{MgB}_2$  [131] and RF measurements have been completed [36].

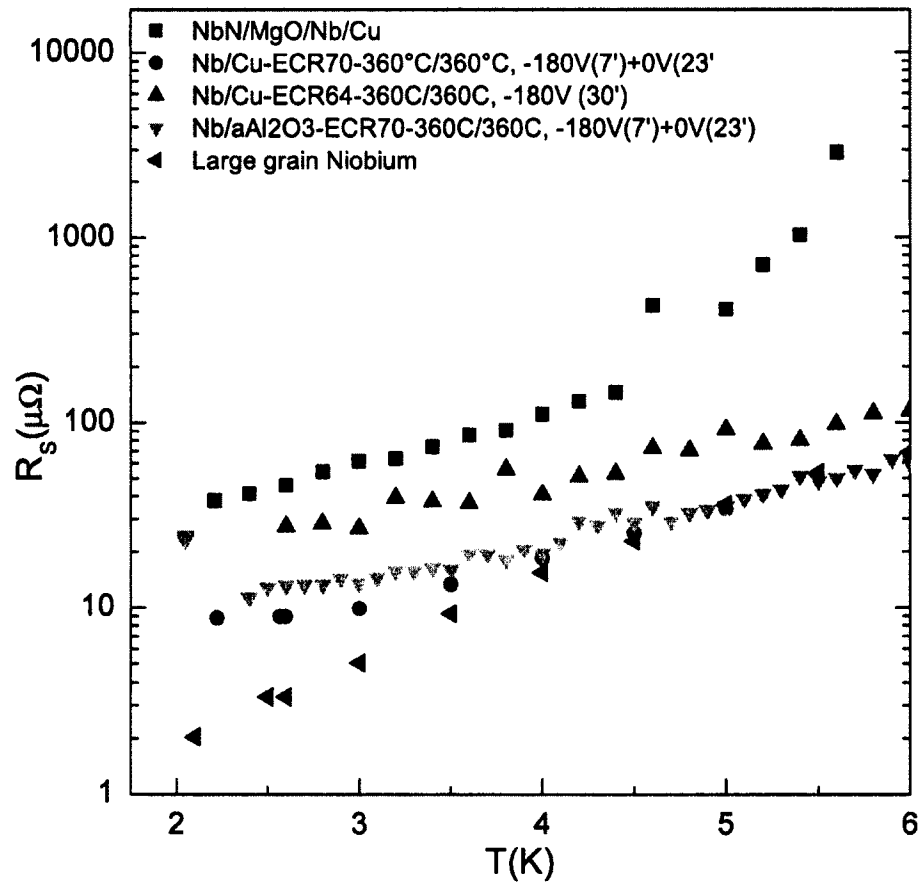


Figure 5.1: Surface resistance as a function of temperature for a NbN/MgO/Nb multilayer, three niobium thin films, and large grain niobium.

These RF measurements can be correlated to other measurement techniques still available for samples this size (such as AFM and XRD). With all of the characterization methods available for this size sample, the question that needs to be answered is 'What materials are best suited for the SIS model?'. There are a number of candidate superconductors (NbN, Nb<sub>3</sub>Sn, MgB<sub>2</sub>, and more exotic ones such as the Fe-based pnictides. . . ) as well as insulators (MgO, AlN, Al<sub>2</sub>O<sub>3</sub>. . . ) that can be used in the multilayer coatings. By correlating the properties that are important to SRF applications like critical fields and surface resistance, it may be possible to determine whether one material is better suited over others. If there is a clear front runner at this point, efforts can be focused on scaling up the deposition process for that material to begin coating cavities.

As part of the scaling up process, dummy cavities could be fabricated that allow witness samples such as coupons or other small samples to be mounted on their interior. These witness samples can be used to determine uniformity of the coating as well as determining the properties of particular regions within the cavity. Additionally, these witness samples could be small enough to use the characterization methods described in this dissertation so that material properties resulting from the deposition can be studied without employing destructive techniques that can also affect material performance. Once the scaling up process is completed, the final test of the model will be to deposit an SIS coating onto the interior surface of a cavity and test its ultimate SRF performance.

There is still a great deal of work to be done before we can answer the ultimate

question of 'Does Gurevich's model work?'. However, based on the work presented in this dissertation and the ongoing work of others, the outlook for the success of the model looks very promising.

# Bibliography

- [1] S. CALATRONI, *Physica C* **441**, 95 (2006).
- [2] J. HALBRITTER, *J. Appl. Phys.* **97**, 083904 (2005).
- [3] J. HALBRITTER, *Supercond. Sci. Technol.* **12**, 883 (1999).
- [4] J. KNOBLOCH, R. L. GENG, M. LIEPE, and H. PADAMSEE, *Proceedings of 1999 Workshop on RF Superconductivity*, TUA004 (1999).
- [5] H. PADAMSEE, J. KNOBLOCH, and T. HAYS, *RF Superconductivity for Accelerators*, Wiley-VCH, second edition, 2008.
- [6] A. GUREVICH, *Appl. Phys. Lett.* **88**, 012511 (2006).
- [7] H. K. ONNES, *Comm. Leiden.* **125c** (1911).
- [8] J. FILE and R. G. MILLS, *Phys. Rev. Lett.* **10**, 93 (1963).
- [9] W. MEISSNER and R. OCHSENFELD, *Die Naturwissenschaften* **21**, 787 (1933).
- [10] F. LONDON and H. LONDON, *Proc. Roy. Soc. London* **A149**, 71 (1935).
- [11] L. V. SHUBNIKOV, V. I. KHOTKEVICH, Y. D. SHEPELEV, and Y. N. RIABININ, *Zh. Eksp. Teor. Fiz.* **7**, 221 (1937).
- [12] A. A. ABRIKOSOV, *J. Exp. Theor. Phys.* **5**, 1174 (1957).
- [13] U. ESSMANN and H. TRÄUBLE, *J. Sci. Instrum.* **43**, 344 (1966).
- [14] U. ESSMANN and H. TRÄUBLE, *Phys. Lett.* **24 a**, 526 (1967).
- [15] V. L. GINZBURG and L. D. LANDAU, *Zh. Eksp. Teor. Fiz.* **20**, 1064 (1950).
- [16] A. B. PIPPARD, *Proc. Roy. Soc. London* **A216**, 547 (1953).
- [17] J. B. KETTERSON and S. N. SONG, *Superconductivity*, Cambridge University Press, 1999.
- [18] J. BARDEEN, L. N. COOPER, and J. R. SCHRIEFFER, *Phys. Rev.* **106**, 162 (1957).
- [19] J. BARDEEN, L. N. COOPER, and J. R. SCHRIEFFER, *Phys. Rev.* **108**, 1175 (1957).

- [20] P. SCHMÜSER, *CERN Accelerator School: Superconductivity and Cryogenics for Accelerators and Detectors CERN-2004-008*, 39 (2004).
- [21] J. HALBRITTER, *Z. Physik* **238**, 466 (1970).
- [22] F. PALMER, *Proc. 3rd Workshop on RF Superconductivity* , 309 (1988).
- [23] J. MATRICON and D. SAINT-JAMES, *Phys. Lett. A* **24**, 241 (1967).
- [24] T. YOGI, G. J. DICK, and J. E. MERCEREAU, *Phys. Rev. Lett.* **39**, 826 (1997).
- [25] H. PADAMSEE, K. W. SHEPARD, and R. SUNDELIN, *Annu. Rev. Nucl. Part. Sci.* **43**, 635 (1993).
- [26] P. KNEISEL, G. R. MYENI, G. CIOVATI, J. SEKUTOWICZ, and T. CARNEIRO, *Proceedings of 2005 Particle Accelerator Conference* , TPPT076 3991 (2005).
- [27] R. L. GENG, G. V. EREMEEV, H. PADAMSEE, and V. D. SHEMELIN, *Proceedings of 2007 Particle Accelerator Conference* , WEPMS006 2337 (2007).
- [28] G. STEJIC, A. GUREVICH, E. KADYROV, D. CHRISTEN, R. JOYNT, and D. C. LARBALESTIER, *Phys. Rev. B* **49**, 1274 (1994).
- [29] C. Z. ANTOINE, S. BERRY, S. BOUAT, J.-F. JACQOUT, J.-C. VILLEGIER, G. LAMURA, and A. GUREVICH, *Phys. Rev. ST Accel. Beams* **13**, 121001 (2010).
- [30] C. Z. ANTOINE, S. BERRY, M. AURINO, J.-F. JACQOUT, J.-C. VILLEGIER, G. LAMURA, and A. ANDREONE, *IEEE Trans. Appl. Supercond.* **21**, 2601 (2011).
- [31] A.-M. VALENTE-FELCIANO, H. L. PHILLIPS, C. E. REECE, J. K. SPRADLIN, K. SEO, A. D. BATCHELOR, F. STEVIE, and R. A. LUKASZEW, *Proceedings of SRF2011* , THPO074 (2011).
- [32] J. NAGAMATSU, N. NAKAGAWA, T. MURANAKA, Y. ZENITANI, and J. AKIMITSU, *Nature* **410**, 63 (2001).
- [33] E. W. COLLINS and M. D. SUMPTION, *Supercond. Sci. Technol.* **17**, S595 (2004).
- [34] X. X. XI, *Supercond. Sci. Technol.* **22**, 043001 (2009).
- [35] M. KRISHNAN, B. BURES, K. WILSON ELLIOT, J. JIANG, A. GUREVICH, D. C. LARBALESTIER, A.-M. VALENTE-FELICIANO, L. PHILLIPS, and C. REECE, *Proceedings of SRF2009* , TUPPO068 (2009).
- [36] B. P. XIAO, X. ZHAO, J. SPRADLIN, C. E. REECE, M. J. KELLEY, T. TAN, and X. X. XI, *Supercond. Sci. Technol.* **25**, 095006 (2012).
- [37] C. ZHUANG, T. TAN, A. KRICK, Q. LEI, K. CHEN, and X. X. XI, *J. Supercond. Nov. Magn.* **26**, 1563 (2013).

- [38] D. BOWRING and L. PHILLIPS, *Proceedings of SRF2009* , TUPPO043 (2009).
- [39] B. P. XIAO, C. E. REECE, H. L. PHILLIPS, R. L. GENG, H. WANG, F. MARHAUSER, and M. J. KELLEY, *Rev. Sci. Instrum.* **82**, 056104 (2011).
- [40] S. AULL, S. CALATRONI, S. DOEBERT, T. JUNGINGER, A. P. EHIASARIAN, J. KNOBLOCH, and G. TEREZIANI, *Proceedings of IPAC2013* , WEPWO044 (2013).
- [41] C. BENVENUTI, S. CALATRONI, M. HAKOVIRTA, H. NEUPERT, M. PRADA, and A.-M. VALENTE, *Proceedings of the 10th Workshop on RF Superconductivity* , MA002, 252 (2001).
- [42] R. F. BUNSHAH, *Handbook of Deposition Technologies for Films and Coatings*, Noyes Publications, second edition, 1994.
- [43] B. WINDOW, *Surf. Coat. Technol* **71**, 93 (1995).
- [44] J. G. HAN, *J. Phys. D* **42**, 043001 (2009).
- [45] A. ANDERS, R. J. MENDELSBERG, S. LIM, M. MENTINK, J. L. SLACK, J. G. WALLIG, A. V. NOLLAU, and G. YU, *Proceedings of SRF2011* , TUIOA06 (2011).
- [46] A. ANDERS, *Thin Solid Films* **518**, 4087 (2010).
- [47] A.-M. VALENTE-FELCIANO, H. L. PHILLIPS, C. E. REECE, J. SPRADLIN, X. ZHAO, and B. XIAO, *Proceedings of IPAC2011* , WEPPC097 (2012).
- [48] M. KRISHNAN, E. VALDERRAMA, C. JAMES, X. ZHAO, J. SPRADLIN, A-M VALENTE-FELICIANO, L. PHILLIPS, C. REECE, K. SEO, Z. H. SUNG, F. A. STEVIE, P. MAHESHWARI, and D. BATCHELOR, *Proceedings of SRF2011* , TUIOB01 (2011).
- [49] T. PROSLIER, J. ZASADZINSKI, J. MOORE, M. PELLIN, J. ELAM, L. COOLEY, C. ANTOINE, J. NOREM, and K. E. GRAY, *Appl. Phys. Lett.* **93**, 192504 (2008).
- [50] S. NISHIKAWA and S. KIKUCHI, *Proc. Imp. Acad. Jpn* **4**, 475 (1928).
- [51] S. NISHIKAWA and S. KIKUCHI, *Nature* **121**, 1019 (1928).
- [52] M. OHRING, *Materials Science of Thin Films*, Academic Press, second edition, 2001.
- [53] A. Y. CHO, *J. Vac. Sci. Technol.* **8**, S31 (1971).
- [54] H. R. GUTIÉRREZ, M. A. COTTA, and M. M. G. DE CARVALHO, *Appl. Phys. Lett.* **79**, 3854 (2001).
- [55] K. PELHOS, T. E. MADEY, J. B. HANNON, and G. L. KELLOGG, *Surf. Rev. Lett.* **6**, 767 (1999).



- [56] J. E. MAHAN, K. M. GEIB, G. Y. ROBINSON, and R. G. LONG, *J. Vac. Sci. Technol. A* **8**, 3692 (1990).
- [57] A. ICHIMIYA and P. I. COHEN, *Reflection High-Energy Electron Diffraction*, Cambridge University Press, 2011.
- [58] G. BINNIG and H. ROHRER, *Helv. Phys. Acta* **55**, 726 (1982).
- [59] G. BINNIG, H. ROHRER, CH. GERBER, and E. WEIBEL, *Phys. Rev. Lett.* **50**, 120 (1983).
- [60] G. BINNIG, C. F. QUATE, and CH. GERBER, *Phys. Rev. Lett.* **56**, 930 (1986).
- [61] I. HORCAS, R. FERNÁNDEZ, J. M. GÓMEZ-RODRÍGUEZ, J. COLCHERO, J. GÓMEZ-HERRERO, and A. M. BARO, *Rev. Sci. Instrum.* **78**, 013705 (2007).
- [62] H. TIAN, G. RIBEILL, C. XU, C. E. REECE, and M. J. KELLEY, *Appl. Surf. Sci.* **257**, 4781 (2011).
- [63] C. XU, H. TIAN, C. E. REECE, and M. J. KELLEY, *Phys. Rev. ST Accel. Beams* **14**, 123501 (2011).
- [64] C. XU, H. TIAN, C. E. REECE, and M. J. KELLEY, *Phys. Rev. ST Accel. Beams* **15**, 043502 (2012).
- [65] W. L. BRAGG, *Proc. Camb. Phil. Soc.* **17**, 43 (1913).
- [66] P. SCHERRER, *Nachr. Ges. Wiss. Göttingen* **26**, 98 (1918).
- [67] L. G. PARRATT, *Phys. Rev.* **95**, 359 (1954).
- [68] M. MCELFRISH, *Quantum Design MPMS Application Notes* (1994).
- [69] B. D. JOSEPHSON, *Phys. Lett.* **1**, 251 (1962).
- [70] P. W. ANDERSON and J. M. ROWELL, *Phys. Rev. Lett.* **10**, 230 (1963).
- [71] C. BÖHMER, G. BRANDSTÄTTER, and H. W. WEBER, *Supercond. Sci. Technol.* **10**, A1 (1997).
- [72] R. RUSSO, L. CATANI, A. CIANCHI, D. DIGIOVENAALÉ, J. LORKIEWICZ, S. TAZZARI, C. GRANATA, P. VENTRELLA, G. LAMURA, and A. ANDREONE, *IEEE Trans. Appl. Supercond.* **19**, 2682 (2009).
- [73] M. AURINO, E. DI GENNARO, F. DI IORIO, A. GAUZZI, G. LAMURA, and A. ANDREONE, *J. Appl. Phys.* **98**, 123901 (2005).
- [74] G. LAMURA, M. AURINO, A. ANDREONE, and J. C. VILLEGIER, *J. Appl. Phys.* **106**, 053903 (2009).
- [75] W. M. ROACH, D. B. BERINGER, J. R. SKUZA, W. A. OLIVER, C. CLAVERO, C. E. REECE, and R. A. LUKASZEW, *Phys. Rev. ST Accel. Beams* **15**, 062002 (2012).

- [76] C. CLAVERO, D. B. BERINGER, W. M. ROACH, J. R. SKUZA, K. C. WONG, A. D. BATCHELOR, and R. A. LUKASZEW, *Cryst. Growth. Des.* **12**, 2588 (2012).
- [77] W. M. ROACH, J. R. SKUZA, D. B. BERINGER, Z. LI, C. CLAVERO, and R. A. LUKASZEW, *Supercond. Sci. Technol.* **25**, 125016 (2012).
- [78] W. M. ROACH, D. B. BERINGER, Z. LI, C. CLAVERO, and R. A. LUKASZEW, *IEEE Trans. Appl. Supercond.* **23**, 8600203 (2013).
- [79] R. RUSSO, *Meas. Sci. Technol.* **18**, 2299 (2007).
- [80] Y. IGARASHI and M. KANAYAMA, *J. Appl. Phys.* **57**, 849 (1985).
- [81] G. OYA, M. KOISHI, and Y. SAWADA, *J. Appl. Phys.* **60**, 1440 (1986).
- [82] K. YOSHII, H. YAMAMOTO, K. SAIKI, and A. KOMA, *Phys. Rev. B* **52**, 13570 (1995).
- [83] K. MAŠEK and V. MATOLIN, *Vacuum* **61**, 217 (2001).
- [84] R. EL-KHOZONDAR, H. EL-KHOZONDAR, G. GOTTSTEIN, and A. ROLLET, *Egypt J. Solids* **29**, 35 (2006).
- [85] J. SOSNIAK and G. W. HILL, *J. Appl. Phys.* **38**, 4390 (1967).
- [86] A. F. MAYADAS, R. B. LAIBOWITZ, and J. J. CUOMO, *J. Appl. Phys.* **43**, 1287 (1972).
- [87] A. F. MAYADAS and M. SHATZKES, *Phys. Rev. B* **1**, 1382 (1970).
- [88] M. KRISHNAN, E. VALDERRAMA, B. BURES, K. WILSON-ELLIOT, X. ZHAO, L. PHILLIPS, A.-M. VALENTE-FELICIANO, J. SPRADLIN, C. REECE, and K. SEO, *Supercond. Sci. Technol.* **24**, 115002 (2011).
- [89] D. B. BERINGER, W. M. ROACH, C. CLAVERO, C. E. REECE, and R. A. LUKASZEW, *Phys. Rev. ST Accel. Beams* **16**, 022001 (2013).
- [90] D. K. FINNEMORE, T. F. STROMBERG, and C. A. SWENSON, *Phys. Rev.* **149**, 231 (1966).
- [91] S. B. ROY, G. R. MYNENI, and V. C. SAHNI, *Supercond. Sci. Technol.* **21**, 065002 (2008).
- [92] C.-A. CHANG, J. C. LIU, and J. ANGILIELLO, *Appl. Phys. Lett* **57**, 2239 (1990).
- [93] R. A. LUKASZEW, Y. SHENG, C. UHER, and R. CLARKE, *Appl. Phys. Lett.* **76**, 724 (2000).
- [94] R. A. LUKASZEW, V. STOICA, C. UHER, and R. CLARKE, *MRS Proceedings* **648** (2000).

- [95] L. STOLT, A. CHARAI, F. M. D'HEURLE, P. M. FRYER, and J. M. E. HARPER, *J. Vac. Sci. Technol. A* **9**, 1501 (1991).
- [96] A. R. WILDES, J. MAYER, and K. THEIS-BRÖHL, *Thin Solid Films* **401**, 7 (2001).
- [97] V. ODERNO, C. DUFOUR, K. DUMESNIL, A. M. P. MANGIN, and G. MARCHAL, *Philos. Mag. Lett.* **78**, 419 (1998).
- [98] E. J. GRIER, M. L. JENKINS, A. K. PETFORD-LONG, R. C. C. WARD, and W. M. R., *Thin Solid Films* **358**, 94 (2000).
- [99] G. WU, A. M. VALENTE, H. L. PHILLIPS, H. WANG, A. T. WU, T. J. RENK, and P. PROVENCIO, *Thin Solid Films* **489**, 56 (2005).
- [100] X. ZHAO, L. PHILLIPS, C. E. REECE, K. SEO, M. KRISHNAN, and E. VALDERRAMA, *J. Appl. Phys.* **110**, 033523 (2011).
- [101] F. GÖMÖRY, *Supercond. Sci. Technol.* **10**, 523 (1997).
- [102] R. SINGH, R. LAL, U. C. UPRETI, D. K. SURI, A. V. NARLIKAR, V. P. S. AWANA, J. ALBINO AGUIAR, and M. SHAHABUDDIN, *Phys. Rev. B* **55**, 1216 (1997).
- [103] J. R. GAVALER, J. K. HULM, M. A. JANOCKO, and C. K. JONES, *J. Vac. Sci. Technol* **6**, 177 (1968).
- [104] R. B. VAN DOVER, D. D. BACON, and W. R. SINCLAIR, *Appl. Phys. Lett.* **41**, 764 (1982).
- [105] S. A. WOLF, I. L. SINGER, E. J. CUKAUSKAS, T. L. FRANCAVILLA, and E. F. SKELTON, *J. Vac. Sci. Technol* **17**, 411 (1980).
- [106] E. J. CUKAUSKAS, W. L. CARTER, and S. B. QADRI, *J. Appl. Phys.* **57**, 2538 (1985).
- [107] R. E. TREECE, M. S. OSOFSKY, E. F. SKELTON, S. B. QADRI, J. S. HORWITZ, and D. B. CHRISEY, *Phys. Rev. B* **51**, 9356 (1995).
- [108] S. SINGARAVELU, J. M. KLOPF, G. KRAFFT, and M. J. KELLEY, *J. Vac. Sci. Technol. B* **29**, 061803 (2011).
- [109] H. DIEPERS, O. SCHMIDT, H. MARTENS, and F. S. SUN, *Phys. Lett. A* **37**, 139 (1971).
- [110] P. KNEISEL, R. W. RÖTH, and H.-G. KÜRSCHNER, *Proceedings of 1995 Workshop on RF Superconductivity*, SRF95C17 (1995).
- [111] M. RAŠKOVIĆ, J. UPDADHYAY, L. VUŠKOVIĆ, S. POPOVIĆ, A.-M. VALENTE-FELICIANO, and L. PHILLIPS, *Phys. Rev. ST Accel. Beams* **13**, 112001 (2010).
- [112] F. WU, S. G. JALOVIAR, D. E. SAVAGE, and M. G. LAGALLY, *Phys. Rev. Lett.* **71**, 4190 (1993).

- [113] K. E. JOHNSON, D. D. CHAMBLISS, R. J. WILSON, and S. CHIAN, *J. Vac. Sci. Technol. A* **11**, 1654 (1993).
- [114] M. HOHAGE, M. BOTT, M. MORGENSTERN, Z. ZHANG, T. MICHELY, and G. COMSA, *Phys. Rev. Lett.* **76**, 2366 (1996).
- [115] D. E. JESSON, K. M. CHEN, S. J. PENNYCOOK, T. THUNDAT, and R. J. WARMACK, *Phys. Rev. Lett.* **77**, 1330 (1996).
- [116] X. GE and K. MORGENSTERN, *Phys. Rev. B* **85**, 045417 (2012).
- [117] H. BRUNE, K. BROMANN, H. RÖDER, K. KERN, J. JACOBSEN, P. STOLTZE, K. JACOBSEN, and J. NØRSKOV, *Phys. Rev. B* **52**, R14380 (1995).
- [118] I. PETROV, P. B. BARNA, L. HULTMAN, and J. E. GREENE, *J. Vac. Sci. Technol. A* **21**, S117 (2003).
- [119] M. RUSANEN, I. T. KOPONEN, J. HEINONEN, and T. ALA-NISSILA, *Phys. Rev. Lett.* **86**, 5317 (2001).
- [120] S. RATH, D. PARAMANIK, S. N. SARANGI, S. VARMA, and S. N. SAHU, *Phys. Rev. B* **72**, 2054110 (2005).
- [121] M. S. WONG, W. D. SPROUI, X. CHU, and S. A. BARNET, *J. Vac. Sci. Technol. A* **11**, 1528 (1993).
- [122] V. I. IVASHCHENKO, P. E. A. TURCHI, and E. I. OLIFAN, *Phys. Rev. B* **82**, 054109 (2010).
- [123] G. EREMEEV, *Proc. SRF 2009*, TUOBAU08 (2009).
- [124] D. D. BACON, A. T. ENGLISH, S. NAKAHARA, F. G. PETERS, H. SCHREIBER, W. R. SINCLEAR, and R. B. DOVER, *J. Appl. Phys.* **54**, 6509 (1983).
- [125] E. I. ISAEV, S. I. SIMAK, I. A. ABRIKOSOV, R. AHUJA, Y. K. VEKILOV, M. I. KATSNELSON, A. I. LICHTENSTEIN, and B. JOHANSSON, *J. Appl. Phys.* **101**, 123519 (2007).
- [126] F. MARSILI, D. BITAULD, A. FIORE, A. GAGGERO, F. MATTIOLI, R. LEONI, M. BENKAHOUL, and F. LÉVY, *Opt. Express* **16**, 3191 (2008).
- [127] H. C. JONES, *Appl. Phys. Lett.* **27**, 471 (1975).
- [128] A. LASCIALFARI, A. RIGAMONTI, E. BERNARDI, M. CORTI, A. GAUZZI, and J. C. VILLEGIER, *Phys. Rev. B* **80**, 104505 (2009).
- [129] A. SHOJI, S. KIRYU, and S. KOHJIRO, *Appl. Phys. Lett.* **60**, 1624 (1992).
- [130] B. J. FEENSTRA, F. C. KLAASEN, D. VAN DER MAREL, Z. H. BARBER, R. PEREZ PINAYA, and M. DECROUX, *Physica C* **278**, 213 (1997).
- [131] T. TAN, C. ZHUANG, A. KRICK, K. CHEN, and X. X. XI, *IEEE Trans. Appl. Supercond.* **23**, 7500304 (2012).